



# Mechanical properties of carbon nanotubes and nanofibers

Henrik Jackman

Faculty of Technology and Science

Physics

Karlstad University Studies | 2012:18

# Mechanical properties of carbon nanotubes and nanofibers

Henrik Jackman

Mechanical properties of carbon nanotubes and nanofibers

---

Henrik Jackman

---

LICENTIATE THESIS

---

Karlstad University Studies | 2012:18

---

ISSN 1403-8099

---

ISBN 978-91-7063-422-2

---

© The author

---

Distribution:

Karlstad University

Faculty of Technology and Science

Physics

SE-651 88 Karlstad, Sweden

+46 54 700 10 00

---

Print: Universitetstryckeriet, Karlstad 2012

---

**WWW.KAU.SE**

---

## Abstract

Carbon nanotubes (CNTs) have extraordinary electrical and mechanical properties, and many potential applications have been proposed, ranging from nanoscale devices to reinforcement of macroscopic structures. However, due to their small sizes, characterization of their mechanical properties and deformation behaviours are major challenges.

Theoretical modelling of deformation behaviours has shown that multi-walled carbon nanotubes (MWCNTs) can develop ripples in the walls on the contracted side when bent above a critical curvature. The rippling is reversible and accompanied by a reduction in the bending stiffness of the tubes. This behaviour will have implications for future nanoelectromechanical systems (NEMS). Although rippling has been thoroughly modelled there has been a lack of experimental data thus far.

In this study, force measurements have been performed on individual MWCNTs and vertically aligned carbon nanofibers (VACNFs). This was accomplished by using a custom-made atomic force microscope (AFM) inside a scanning electron microscope (SEM). The measurements were done by bending free-standing MWCNTs/VACNFs with the AFM sensor in a cantilever-to-cantilever fashion, providing force-displacement curves. From such curves and the MWCNT/VACNF dimensions, measured from SEM-images, the critical strain for the very onset of rippling and the Young's modulus,  $E$ , could be obtained. To enable accurate estimations of the nanotube diameter, we have developed a model of the SEM-image formation, such that intrinsic diameters can be retrieved.

We have found an increase in the critical strain for smaller diameter tubes, a behaviour that compares well with previous theoretical modelling. VACNFs behaved very differently, as they did not display any rippling and had low bending stiffnesses due to inter-wall shear. We believe that our findings will have implications for the design of future NEMS devices that employ MWCNTs and VACNFs.

---

---

## List of publications

This thesis is based on the work done in the following appended publications:

- I *Measurements of the critical strain for rippling in carbon nanotubes* H. Jackman, P. Krakhmalev, and K. Svensson, Applied Physics Letters 98, 183104 (2011).
- II *Image formation mechanisms in scanning electron microscopy of carbon nanotubes, and retrieval their of intrinsic dimensions* H. Jackman, P. Krakhmalev, and K. Svensson, *Submitted to Ultramicroscopy (2011-12-12)*.
- III *Direct measurement of bending stiffness and estimation of Youngs modulus of vertically aligned carbon nanofibers* F. A. Ghavanini, H. Jackman, K. Svensson, P. Lundgren, and P. Enoksson, *In manuscript*.

The author of this thesis was responsible for most of the writing and carried out the experimental work and analysis in publications I and II.

In publication III, the contribution from the author was performing the mechanical measurements and doing some of the analysis.

---

# Contents

<b>Acronyms</b>	<b>v</b>
<b>1 Introduction</b>	<b>1</b>
<b>2 Background</b>	<b>5</b>
2.1 History . . . . .	5
2.2 Carbon structures . . . . .	6
2.3 Structure of CNTs . . . . .	7
2.4 Properties . . . . .	8
2.4.1 Electronic properties . . . . .	8
2.4.2 Mechanical properties . . . . .	9
2.5 Applications . . . . .	11
2.5.1 Electrical . . . . .	11
2.5.2 Mechanical . . . . .	11
2.5.3 Nanoelectromechanical systems . . . . .	12
<b>3 Experimental</b>	<b>15</b>
3.1 Scanning electron microscopy . . . . .	15
3.1.1 Electron gun . . . . .	15
3.1.2 Electromagnetic lenses . . . . .	17
3.1.3 Beam-specimen interaction . . . . .	19
3.1.4 Beam interaction with carbon nanotubes . . . . .	20
3.1.4.1 Simulation . . . . .	23
3.2 In situ SEM-AFM . . . . .	28
3.2.1 Calibrating the in situ SEM-AFM . . . . .	28



## CONTENTS

---

<b>4</b>	<b>Materials</b>	<b>31</b>
4.1	Synthesis methods . . . . .	31
4.1.1	Arc discharge . . . . .	31
4.1.2	Laser ablation . . . . .	32
4.1.3	Chemical vapor deposition . . . . .	32
4.2	Materials used . . . . .	33
4.2.1	CVD-grown carbon nanotubes . . . . .	33
4.2.2	Vertically aligned carbon nanofibers . . . . .	34
<b>5</b>	<b>Mechanical properties</b>	<b>37</b>
5.1	Previous work . . . . .	37
5.1.1	Experimental . . . . .	37
5.1.2	Theoretical . . . . .	42
5.2	In situ SEM-AFM bending experiments . . . . .	44
5.2.1	Multi-walled carbon nanotubes . . . . .	44
5.2.2	Vertically aligned carbon nanofibers . . . . .	49
	<b>Acknowledgements</b>	<b>55</b>
	<b>References</b>	<b>57</b>

# Acronyms

<b>AFM</b>	Atomic force microscopy/microscope
<b>BSE</b>	Backscattered electrons
<b>CCVD</b>	Catalytic chemical vapor deposition
<b>CNF</b>	Carbon nanofiber
<b>CNT</b>	Carbon nanotube
<b>CVD</b>	Chemical vapor deposition
<b>EBID</b>	Electron beam-induced deposition
<b>f-CNT</b>	Functionalized carbon nanotube
<b>FEG</b>	Field emission gun
<b>MD</b>	Molecular dynamics
<b>MWCNT</b>	Multi-walled carbon nanotube
<b>NEMS</b>	Nanoelectromechanical systems
<b>SE</b>	Secondary electron
<b>SEM</b>	Scanning electron microscopy/microscope
<b>SWCNT</b>	Single-walled carbon nanotube
<b>TEM</b>	Transmission electron microscopy/microscope
<b>VACNF</b>	Vertically aligned carbon nanofiber
<b>VLS</b>	Vapor-liquid-solid

CONTENTS

---

# Chapter 1

## Introduction

If not familiar to carbon nanotubes (CNTs) one could, given the name, guess that it is a small tube (nano means a billionth) made up of carbon, and that is just what it is. A single walled carbon nanotube (SWCNT) can be seen as one atomic layer of carbon (graphene) in the shape of a tube. A CNT can also consist of several concentric tubes and is then referred to as multi-walled carbon nanotubes (MWCNTs). The diameter of CNTs ranges from about 1 nm to 100 nm, and their lengths can be up to a couple of centimetres. Their typical length is however a few micrometers.

The large scientific community was introduced to carbon nanotubes in 1991 [1] and since then the interest in this material has been huge. Material scientists, working in the coal, steel, and nuclear industry, had observed hollow nanometer-sized carbon filament well before 1991 [2]. They however lacked high-resolution electron microscopy, making it impossible to determine the nanotube structure. Also, the aim of their work was often to prevent growth of these filaments since they were inhibiting their industrial processes.

Theoretical modelling predicted CNTs to have extraordinary properties, which later has been demonstrated experimentally [3]. Looking at the mechanical properties their Young's modulus has been measured to be about 1 TPa [4], which is 5 times stiffer than steel. Their tensile strength has also been measured and was found to be as high as 150 GPa [5], well exceeding the strength of macroscopical materials. Translating these properties to the macroscopic world, a wire having the size of a human hair could lift a weight of 100 kg. Their density is also low, compared to other materials having high Young's modulus and tensile strength, making their specific modulus and strengths

## 1. INTRODUCTION

---

even larger in comparison to these materials. In addition, CNTs are also very elastic, and they can be stretched and bent severely without obtaining permanent damage. This makes CNTs attractive to use as a fiber composite in future lightweight, high stiffness and strength materials. Though their mechanical properties have not been fully exploited yet, there are CNT containing products available today, e.g. skis, ice hockey sticks, and surf-boards [6].

It has been observed that SWCNTs buckles when bent, much like a straw would, and this buckling was shown to be reversible, i.e. no permanent damage could be observed when straightening the tube. MWCNTs behave differently during bending, since the inner tubes act as a support for the outer tubes, preventing them from buckling. Instead of a single localized collapse, it develops into a distributed pattern of ripples, along the contracted side of the bent CNT (shown in Fig. 1.1). This phenomenon is referred to as the rippling mode. Modelling of this mode has indicated a decrease in the bending stiffness following the rippling onset [7], which would have implications for future applications.

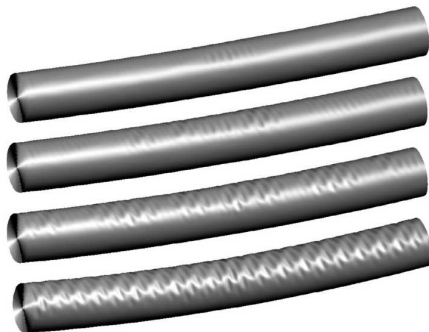


**Figure 1.1:** Images of a modelled 40-walled MWCNT, experiencing rippling. The bending curvature is increased from the topmost to the bottommost tube. Reprinted with permission from [7]. © 2008 Elsevier.

Synthesizing methods can be engineered to obtain vertically aligned carbon nanofibers (VACNF) having a cup-stacked structure, rather than the concentric cylinder structure of CNTs. These fibers are grown from pre-patterned catalyst particles and could find use in future nanoelectromechanical systems (NEMS). In potential NEMS applications, the bending stiffness of the VACNF is one of the most important parameters.

---

Measuring the mechanical properties of individual nanotubes is challenging, as one would like to image the CNT and measure the bending forces simultaneously. A recently developed instrument accomplishes just that [8, 9]. By placing a miniaturized manipulator and force sensor inside an electron microscope, one can characterize individual, free-standing, nanostructures.

In this work we have used a custom-built instrument that effectively joins atomic force microscopy (AFM) with scanning electron microscopy (SEM). This enables direct force measurements on individual free-standing MWCNTs and VACNFs. We can thereby detect the very onset of rippling and study the change in bending stiffness following the rippling onset. We have found that the rippling starts at very low curvatures and that small diameter tubes have a rippling onset at higher strains compared to large diameter tubes. There were also indications that the critical strain depends on the defect density in the MWCNTs. A higher defect density leads to a lower Young's modulus and a higher resistance against rippling. In VACNF, where the graphene layers are not parallel to the fiber axis, shear between the layers will govern the mechanical properties. The fibers thereby have a very low Young's modulus and do not display any rippling. These findings will have implications for the design of future NEMS applications.

## 1. INTRODUCTION

---

## Chapter 2

# Background

### 2.1 History

"Carbon nanotubes (CNTs) were first discovered in 1991 by Iijima [1]" is a common phrase in a manuscript concerning CNTs. There is however a debate regarding who should be credited for the discovery of carbon nanotubes [2]. Filamentous growth of carbon from thermal decomposition of gaseous hydrocarbon had been suggested over 100 years before the famous paper by Iijima. At that time no microscope was able to resolve details smaller than a few micrometers. With the invention of transmission electron microscopy (TEM) details on the nanoscale could be imaged and in 1952 a Soviet Union research group published a paper showing TEM micrographs of hollow tubular carbon filaments with a diameter in the range of 50 nm [10], most probably the first TEM images of a multi-walled CNT (MWCNT). Being the first to publish such images, the authors of [2] claim that Radushkevich and Lukyanovich should be credited for the discovery of CNTs. But the paper by Radushkevich and Lukyanovich did not spark any major interest. For this there are many reasons. For one the paper was published in a journal not easily accessible outside the Soviet Union. Also the research on this topic was performed in order to prevent the growth of such filaments in steel industry processing and in the coolant channels of nuclear reactors.

Iijima's paper was published in *Nature*, a journal read by a broad scientific public. It was published in a time when the interest in carbon from fundamental physicists was big, following the discovery of the  $C_{60}$  molecule in 1985 [11], a work that was awarded with the Nobel prize in chemistry in 1996. All of these circumstances contributed to



## 2. BACKGROUND

---

the big impact the paper have had. In the paper TEM images and diffraction patterns of individual MWCNTs were published along with a description of their concentric cylinder structure of graphene layers. Two years later Iijima and Ichihashi [12] and another group, Bethune et al. [13], published two independent papers showing the first TEM images of single-walled carbon nanotubes (SWCNTs), further increasing the interest in CNTs.

### 2.2 Carbon structures

A free carbon atom has the electron configuration  $1s^2 2s^2 2p^2$ , where the energy difference between the 2s and 2p orbitals is comparatively small. The small difference enables the wavefunctions of these orbitals to mix when binding to other atoms, thereby increasing the binding energy. Mixing of the orbitals forms new basis sets called hybridizations that are then filled with electrons. When one 2s state mixes with  $n$  2p states it is called  $sp^n$  hybridization, where  $n = 1, 2, 3$ . Carbon atoms bound together with a  $sp^1$  hybridization will form a 1D chain structure with two electrons in two  $\sigma$  bonds and two electrons in two  $\pi$  bonds per atom. When carbon binds with a  $sp^2$  hybridization three electrons will form three  $\sigma$  bonds and one electron will form one  $\pi$  bond. In  $sp^3$  hybridization all four valence electrons will contribute to four  $\sigma$  bonds. The  $\sigma$  bonds are strong and localized, whereas the  $\pi$  bonds are weaker and less localized. This means that electrons in  $\pi$  and  $\pi^*$  bonds can move between the atoms while electrons in a  $\sigma$  bond are fixed at one atom.

Diamond is an allotrope of carbon where the atoms have  $sp^3$  bonds, giving diamond its exceptional physical properties. Diamond is the hardest material known, with an extremely high thermal conductivity. It also has a large bandgap (5.5 eV), making it an electrical insulator and transparent to visible light. Graphite is another allotrope with the difference that the atoms have  $sp^2$  bonds, making graphite a layered material. The atoms are arranged in a honeycomb patterned, forming atomic planes that can be stacked in a hexagonal (ABAB), rhombohedral (ABCABC) or in a turbostratic (randomly stacked) fashion. The inter-planar distance depends on the stacking. Hexagonal and turbostratic graphite have the smallest (3.354 Å) and largest (3.440 Å) inter-planar distance respectively.

In the planes the atoms have  $\sigma$  and  $\pi$  bonds, while between the planes there are only van der Waals forces, resulting in a very anisotropic material. The intraplane electrical and thermal conductivities are high whereas the interplane counterparts are low. It is similar with the mechanical properties, where the stiffness and strength within a plane are high but very low between the planes. This allows graphite planes to slide past each other easily, making graphite a useful solid lubricant. These mechanical properties are also made use of when writing with a pencil, where graphite layers are easily stripped from the pencil and attached to the paper.

Another allotrope is graphene, for which the demonstration and characterisation of [14] was awarded the Nobel in physics prize in 2010. Novoselov and Geim also exploited the weak bond between graphite layers when obtaining their graphene flakes. Starting with platelets of highly-oriented pyrolytic graphite they peeled off graphene flakes simply using scotch tape. The flakes were characterized showing that graphene is a 2D semimetal, stable under ambient conditions (previously believed to be impossible) [14]. Graphene is a 2D material with extraordinary properties and has since the discovery sparked an enormous interest, partly because of its similarity to carbon nanotubes.

## 2.3 Structure of CNTs

As stated previously MWCNT are concentric cylinders of graphene and the structure suggested by Iijima in 1991 [1] has later been confirmed and is often described using the chiral vector,  $\vec{C}$ :

$$\vec{C} = n\vec{a}_1 + m\vec{a}_2 \quad (2.1)$$

where  $n$  and  $m$  are two integers and  $\vec{a}_1$  and  $\vec{a}_2$  are the unit vectors of the hexagonal lattice of the graphene sheet. The chiral vector expresses how the graphene sheet is rolled up to form a SWCNT, and the length of  $\vec{C}$  is the perimeter. Depending on the integers  $n$  and  $m$  a CNT can have various chiralities expressed as  $(n, m)$ , i.e rolled up in different ways. The unit vectors, and how they are used to roll up a SWCNT, are shown in Fig. 2.1 (a) where the chiral vector of a (4,3) SWCNT is shown. There are three distinct types of chiralities: armchair with  $n = m$ , zigzag with  $m = 0$ , and chiral with arbitrary values of  $n$  and  $m$ . Examples of these three types are shown in Fig. 2.1 (b).

## 2. BACKGROUND

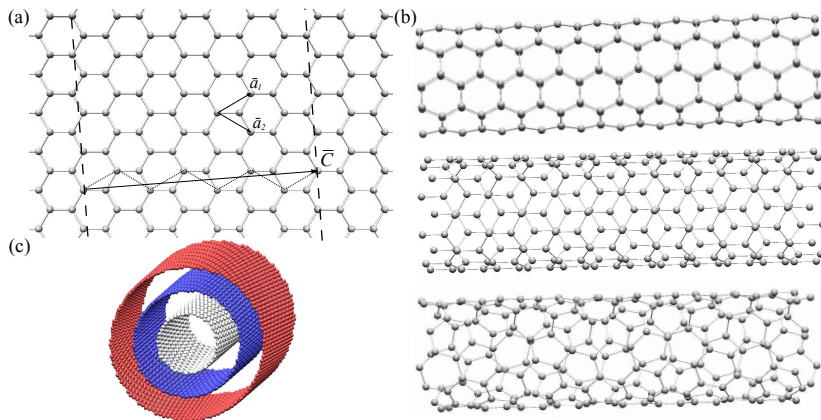


**Figure 2.1:** (a) the unit vectors,  $\vec{a}_1$  and  $\vec{a}_2$ , in a graphene lattice. (b) three types of SWCNT from top to bottom: armchair (5,5), zigzag (9,0), and chiral (7,3). (c) MWCNT constituting of three chiral tubes.

From  $\vec{C}$  the diameter can be obtained and it is given by:

$$d = \frac{\sqrt{3}}{\pi} a_{C-C} (m^2 + mn + n^2)^{1/2} \quad (2.2)$$

where  $a_{C-C}$  is the bond length between the carbon atoms in graphene (1.42 Å).

As mentioned earlier there are also multiwalled carbon nanotubes, consisting of multiple concentric cylinder with a spacing similar to the interplanar spacing in turbostratic graphite (3.440 Å). An example of a MWCNT is shown in Fig. 2.1 (c) where three concentric chiral CNTs constitute a MWCNT. For a more thorough description of the structure see for example [3].

## 2.4 Properties

### 2.4.1 Electronic properties

Soon after the "discovery" of MWCNT in 1991, theoreticians began calculating the electronic structure for the simplified case of SWCNTs. From calculations it was found that the electronic structure depended on the chirality,  $(n, m)$ . CNTs with chirality satisfying the condition:

$$n - m = 3j \quad (2.3)$$

where  $j = 0, 1, 2, \dots$ , were found to be metallic while the CNTs not satisfying the relation were found to be semiconducting [15]. The dependence of the electronic structure on the chirality can be understood by looking at what happens when graphene is folded into a CNT. Graphene is a zero-gap semiconductor where the occupied  $\pi$  band and the unoccupied  $\pi^*$  band meet at Fermi level at the  $K$  point in the Brillouin zone. When folding graphene into a CNT, periodic boundary conditions in the circumferential direction are imposed, resulting in exclusion of many  $\bar{k}$  states. The  $K$  points are excluded if Eq. 2.3 is not satisfied, hence resulting in a semiconducting CNT. These calculations were later verified by performing scanning tunneling spectroscopy on individual SWCNT [16, 17]. Because of their perfect crystal symmetry, SWCNT also act as quantum wires with ballistic conductance and can withstand high current densities [18]. These electronic properties make CNTs an interesting material for future electronic applications.

### 2.4.2 Mechanical properties

The  $sp^2$  bond does not only give CNTs fascinating electrical properties, it is also one of the strongest and stiffest chemical bonds in an extended system known in nature [19]. As for the stiffness, the in plane elastic constant,  $c_{11}$ , of graphite was at the "discovery" of CNTs known to be  $1.06 \pm 0.02$  TPa [20], almost five times that of steel. Since graphite and CNTs both have  $sp^2$  bonding, the mechanical properties of CNTs were predicted to be similar to graphites.

Early theoretical work on the mechanical properties focused on the strain energy per atom [21]. From molecular dynamics, using empirical potentials, it was found that the strain energy increased with decreasing diameter, while approaching the values for graphite at large diameters. This result agrees with the classical result saying that  $E_{strain} \propto 1/d^2$ . In the same work, the stiffness of several SWCNTs was calculated and it was found to be close to  $c_{11}$  of graphite.

Measurements of the mechanical properties on macroscopical materials are often made by mounting a standard specimen of the desired material in an instrument that exerts deformations on the specimen and measures the resulting forces. This becomes difficult for materials on the nanoscale because of the small dimensions. Other methods are therefore needed to determine the mechanical properties of CNTs. An early experimental estimate of the stiffness of MWCNTs was made by looking at the amplitude of their intrinsic thermal vibrations inside a TEM. By assuming the MWCNTs to

## 2. BACKGROUND

---

be cantilevered beams with a circular cross section they obtained a Young's modulus,  $E$ , varying between 0.40-4.15 TPa [22]. The same group later published another paper where they had improved their method and looked solely on SWCNTs where they found a  $E = 1.25^{+0.45}_{-0.35}$  TPa, by using a layer thickness of 0.34 nm [23]. These studies, though having large uncertainty, show the high stiffness of CNTs. However, they do not describe how CNTs will respond to applied loads in an application.

Another study used MWCNTs lying on a substrate, clamped at one end and deflected at the other end with an AFM cantilever. This yielded a force-displacement,  $F - \delta$ , curve, telling how the cantilevered MWCNTs responded to the bending. From these  $F - \delta$  curves the spring constant could be obtained, and together with the outer diameter and length of the MWCNTs, used to calculate Young's modulus. Their obtained Young's modulus was  $E = 1.28 \pm 0.5$  TPa [24]. In addition to this they also saw that MWCNTs could be bent to large curvatures without any irreversible deformation, i.e withstand large deformation elastically. However, at a certain deflection they saw a kink in the  $F - \delta$  curves, after which the spring constant appeared to have decreased. Imaging MWCNTs bent above this deflection revealed a change in topology, where bumps showed up on the cylinder surface. Changes in the internal structure have also been observed in a TEM study of MWCNTs where tubes were statically bent during the sample preparations, and showed signs of buckling [25].

The buckling was further investigated in another TEM study accompanied by molecular dynamics (MD) simulations [26]. The simulations were performed to study the behaviour of bent CNTs and reproduced the buckling pattern for a SWCNT and a DWCNT. They also showed that the strain energy of the CNTs increased linearly when bent past the critical curvature for buckling, equivalent of continuing deformation under a constant force. Another MD study showed similar behaviour of CNTs subjected to bending, and also showed morphology changes of CNTs subjected to twisting and axial compression [27]. This non-linear elastic behaviour allows CNTs to withstand large deformations without any irreversible deformation. Mechanical properties of CNTs will be discussed further in Section 5.1.

## 2.5 Applications

### 2.5.1 Electrical

Many potential applications of CNTs have been proposed as a result of their remarkable properties. Individual metallic SWCNTs have been proposed to function as interconnects for integrated circuits because of their small size, ballistic transport and ability to withstand high current densities [18]. Semiconducting SWCNTs can in turn be used as the channel material in field effect transistors [28]. Devices employing SWCNTs as interconnects and channel material could be smaller, faster and more energy efficient than today's silicon-based devices. However, before having large integrated circuits consisting of SWCNTs, techniques for depositing or growing SWCNTs, with a predefined chirality, are needed [29]. The electronic properties have been exploited to fabricate thin, flexible, and transparent films of SWCNTs [30]. Although bulk samples of CNTs are one of the darkest materials known [31], thin films can have a high transparency. The electrical conduction of these films show little degradation after repeated strain cycles, making them an attractive material to use as transparent electrodes in flexible photovoltaic devices [30].

### 2.5.2 Mechanical

Because of their high stiffness and yield strength together with their low weight, incorporation of CNTs in various matrices have been studied. These composites often show an increase in stiffness and strength but they are far from the properties of individual CNTs [32]. Before one can obtain composites that fully exploits the mechanical properties of CNTs, the bonding between CNTs and the matrix as well as the alignment and dispersion of CNTs in the matrix needs to be improved. These are difficult tasks because of the small dimensions and tendency to bundling of several CNTs through van der Waals forces. Though their mechanical properties have not yet been fully exploited, there are CNT containing products available today, e.g. skis, ice hockey sticks, and surf-boards [6]. The addition of CNTs to these composites mainly increase their strength and toughness, but it can also increase the stiffness.

## 2. BACKGROUND

---

### 2.5.3 Nanoelectromechanical systems

It has been shown that CNTs cantilevered to an electrode will bend towards a counter electrode when a potential is applied between the electrodes, due to an electrostatic force [4]. This phenomenon was used to excite the eigenfrequency of the CNTs. Using this frequency, along with the CNT dimensions, the Young's modulus could be calculated (described in more detail in section 5.1). Because of their small size, low weight, high stiffness, and high electrical conductance it was early proposed to exploit this phenomenon in nanoelectromechanical systems (NEMS). The high stiffness of a clamped CNT enables high operating frequencies since the eigenfrequency,  $\omega$ , of a clamped beam is given by:

$$\omega = B \sqrt{\frac{EI}{\rho A l^4}} \quad (2.4)$$

where  $B$  is a constant depending on the boundary conditions,  $I$  is the moment of inertia,  $\rho$  the density,  $A$  the cross-sectional area, and  $l$  the length of the beam. Cantilevered CNTs can have eigenfrequencies in the gigahertz range, making them an ideal candidate in nanoelectromechanical switching devices [33].

Several NEMS exploiting the electrostatic bending of CNTs have been proposed. In an early article the threshold voltage for a two-terminal switch employing a CNT was studied. Their geometry consisted of a CNT cantilevered to an electrode that was attracted to form a closed circuit to a counter electrode [34]. Though they found low threshold voltages, these voltages would induce large currents in the CNT, in closed circuit. These high currents were avoided in another geometry where an additional gate electrode was used [35]. In this proposed model, pictured in Fig. 2.2 (a), a relatively high voltage is applied between the source (S) and gate (G) electrodes, causing the CNT to bend towards the drain (D) electrode. The source-drain voltage can in this geometry be held relatively low. This model has been further studied and demonstrated [36, 37, 38, 39], though not reaching the predicted gigahertz switching frequencies for various reasons.

In another approach vertically aligned CNTs, as pictured in Fig. 2.2 (b), were used to form a switch. The advantage of using this geometry is that vertically aligned CNTs can be grown from patterned catalysts, simplifying the device production. In this model a large source-gate voltage is applied causing the drain CNT to bend towards the source CNT, while a smaller source-drain voltage is maintained. This device was

demonstrated in [40] and further refined by the same group in [41]. Since then research has been made aiming further simplifying the fabrication of these devices [42, 43].

Other NEMS using the electrostatic bending of CNTs include: double clamped switches [44, 45, 46], atomic-resolution mass sensor [47], and nanotube radio [48] to mention a few.

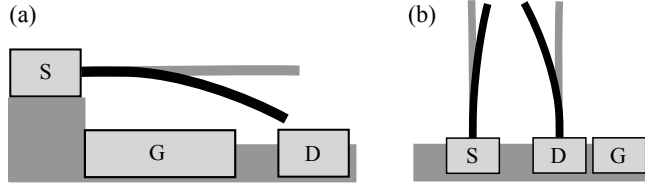


**Figure 2.2:** (a) Nanorelay build up by three electrodes and a CNT on an insulating substrate. By applying a source-gate voltage the CNT is attracted towards the gate and drain electrode [35]. (b) Nanoswitch employing two CNTs and three electrodes. By applying a large voltage, of the same sign as the drain electrode, to the gate electrode the drain CNT will bend towards the source CNT [41].

Modelling of the CNTs and CNFs, in the applications described above, were made by assuming them to be linear elastic beams with a Young's modulus of  $\sim 1$  TPa. However, only defect free CNTs, produced using high temperature methods, show a Young's modulus of 1 TPa, while CNTs grown using catalytic low temperature methods can show Young's moduli two orders of magnitude smaller [49]. It has also been reported that CNTs behave non-linearly when bent at large curvatures, reducing their stiffness [4]. Therefore it is important to characterize the mechanical properties of the materials proposed to be used in future NEMS applications.



## 2. BACKGROUND

---

## Chapter 3

# Experimental

### 3.1 Scanning electron microscopy

An SEM image is obtained by scanning a focused electron beam on a specimen surface, pixel by pixel, and detecting the electrons escaping from this surface. The detected electron intensity,  $I(r)$ , as a function of the lateral coordinates,  $r$ , forms an image, usually displayed in gray-scale where white is maximum intensity. In order to obtain a focused electron beam, an SEM needs to have two components: an electron gun and electron lenses. The components are usually positioned with the gun at the top and the lenses below, ending with the sample at the bottom as illustrated in Fig. 3.1. Different detectors at different positions in the SEM are also illustrated in this figure.

#### 3.1.1 Electron gun

The purpose of the electron gun is to supply the SEM with free electrons accelerated by a voltage,  $V_{acc}$ . Electrons are obtained from a source by overcoming the source materials work function. This can be done by either heating the source (thermionic emission) or by applying a large local electric field at the source (field emission) or by a combination of those two. Thermionic emission guns often consist of a tungsten wire bent into a V-shape as the cathode, often referred to as a hairpin-filament. There are also other thermionic sources, e.g the LaB<sub>6</sub> cathode which has a lower work function compared to tungsten. The hairpin-filament is heated to a temperature of 2000-2700 K and a voltage applied to the anode extracts electrons from the tip. To reduce the emission at large solid angles, the tungsten cathode is surrounded by a Wehnelt element.

### 3. EXPERIMENTAL

---

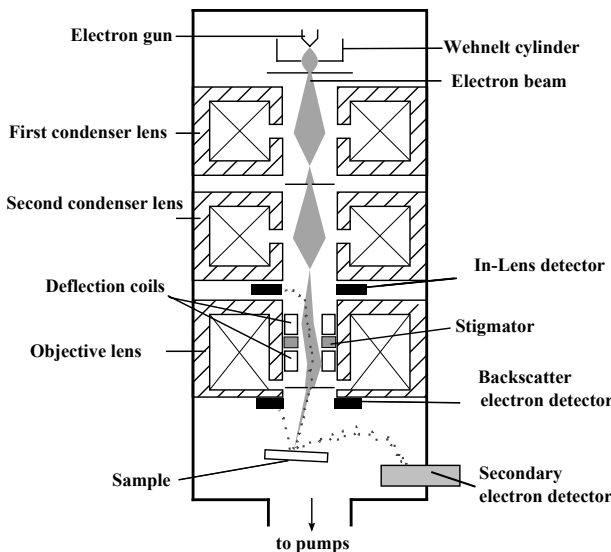


**Figure 3.1:** Schematic sketch of an SEM. Modified from [50].

This element is biased with a slightly negative voltage and acts to focus the emitted electrons into a beam cross-over. Tungsten filaments can supply large beam currents but this current is emitted from a relatively large area requiring a large demagnification from the electron lenses to achieve a small electron probe at the sample. The axial gun brightness  $\beta$ , defined as the current  $\Delta I$  passing through an area  $\Delta A$  into a solid angle  $\Delta\Omega$ :

$$\beta = \frac{\Delta I}{\Delta A \Delta\Omega} \quad (3.1)$$

is relatively low for tungsten filaments. The advantages of these filaments are that they are cheap and stable and do not require as high vacuum when operating as compared to field emission guns.

A field emission gun (FEG) consists of a cathode with a sharp tip ( $r_{tip} < 100$  nm), an anode is used to extract electrons from the cathode and a second anode to accelerate the extracted electrons. The material of the cathode tip is usually single crystal tungsten, because of the dependence of the emitted current on the crystal orientation. Having emittance at large solid angles will cause a lot of electrons to hit the first anode and hence create ions that would be accelerated towards the cathode and damage the source. The (100) direction in tungsten limits the emittance to a cone with a semi-apex angle of about 0.1 rad, thus reducing the probability of electrons hitting the anode. The area from where the electrons are extracted is small compared to a thermionic source. Thereby the need for demagnification of the beam is much smaller. FEG-SEMs routinely gives electron probe sizes of 1 – 5 nm at the sample, enabling high resolution imaging at low acceleration voltages. The brightness of a FEG is two orders of magnitude larger than that of thermionic sources and they also have longer lifetimes. The disadvantage of FEGs is that they are more expensive and less stable than thermionic sources. They also require higher vacuums during operation, and are usually differentially pumped.

#### 3.1.2 Electromagnetic lenses

After the electron gun the electron beam first reaches the condensor lenses and then the objective lens, as illustrated in Fig. 3.1. The purpose of the lens system is to demagnify the source image of the cathode and focus it to a small electron probe on the sample. The demagnification is obtained by focusing off-axis beam electrons towards the optic axes, using electromagnetic lenses, and by excluding electrons far off-axis using apertures. The electromagnetic lenses consist of a coil of wire enclosed by an circular symmetric iron casing. Applying a current to the coil induces a magnetic field,  $\vec{B}$ , that focuses off-axis electrons toward the optic axis through the Lorentz force:

$$\vec{F} = -e (\vec{E} + \vec{v} \times \vec{B}) \quad (3.2)$$

where  $-e$  and  $\vec{v}$  is the charge and velocity of the electron respectively and  $\vec{E}$  is an electric field. Because of this force the electrons focused by the lenses move in spirals down the column. The strength of the condenser lens is normally only changed between predefined settings, often named spot size, by the operator in the controlling software. The aim of the objective lens is to demagnify the beam and to focus the beam on the

### 3. EXPERIMENTAL

---

surface of the sample. The strength of the objective lens is controlled by the operator. Inside this lens the deflection coils, the stigmator and another beam limiting aperture is situated. The deflection coils are the components that scan the beam and the current in these coils determines the magnification of the image. The stigmator applies a weak magnetic field, controlled by the operator, aiming at making the beam circular symmetric. A beam that is not circular symmetric will render an astigmatic image that can be recognized by observing how known circular objects appear stretched in one direction, hence distorting the image and reducing the resolution.

Apart from astigmatism the electromagnetic lenses also suffer from a number of other aberrations. Thus they cannot focus the electron beam into a homogeneous spot on the specimen surface, but rather into a disk of least confusion with diameter  $d_p$ . Spherical aberration occurs in the lenses because electrons further away from the optic axis are affected by a stronger magnetic field than electrons closer to the optic axis. This causes electrons further away from the optic axis to be deflected more resulting in a cross-over earlier in the column. This spherical aberration will result in a disk of least confusion having diameter  $d_s$ , as illustrated in Fig. 3.2.

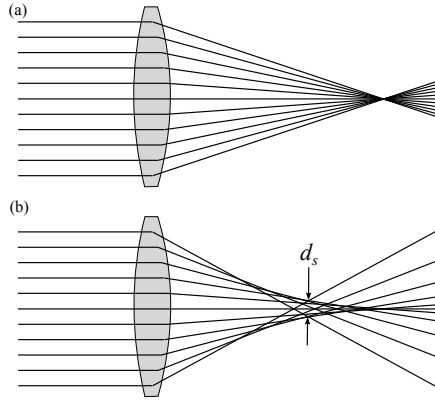


**Figure 3.2:** (a) Schematic of a perfect lens where all off-axis electrons are being focused into a spot. (b) Schematic of a lens suffering from spherical aberration where electrons further away from the optic axis are focused earlier onto the optic axis, resulting in a disk of least confusion, with  $d = d_s$ , instead of a spot.

Not all electrons emitted from the electron gun have the same energy. Because of this energy spread, electrons with a lower energy are focused onto the optic axis earlier in the column. This phenomenon is called chromatic aberration, resulting in a disk of least confusion with diameter  $d_c$ . Another source of imperfection in the lens system is the apertures. For small apertures the beam electrons are diffracted in a circular pattern with diameter  $d_d$ .

Assuming the distribution of these aberrations to be Gaussian and also adding the demagnified diameter of the electron source,  $d_0$ , the total diameter of the electron probe can be written as:

$$d_p = (d_0^2 + d_s^2 + d_d^2 + d_c^2)^{1/2} \quad (3.3)$$

The resolution of an SEM can be as good but never better than  $d_p$  which will be discussed in more detail later. Modern SEM employing a FEG can obtain probe diameters as small as  $d_p = 1$  nm, where the diameter increases with decreasing acceleration voltage.

#### 3.1.3 Beam-specimen interaction

When the beam hits the specimen the electrons will interact with the atoms, consisting of a localized positively charged nuclei and the dispersed negatively charged electrons. Some beam electrons will be scattered elastically at large angles. After a number of such events this can lead to electrons escaping the specimen, retaining much of their initial energy. These electrons are called backscattered electrons (BSE) and have by convention  $E > 50$  eV. The backscattering coefficient, i.e how efficiently a material backscatters electrons, is proportional to the square of the atomic number of the specimen,  $Z^2$ .

While travelling through the specimen, the beam electrons will gradually lose energy through inelastic scattering events, giving rise to secondary electrons (SE) and X-rays. The SEs can be used to form an image of the specimen and the X-rays to get elemental analysis of the specimen. Since the loss of energy is gradual, some electrons can travel large distances within the specimen, repeatedly creating SEs and X-rays, before coming to rest. This results in a large information volume for bulk specimen. Thus even if  $d_p$  is small, the information volume is large, reducing the image resolution as illustrated in Fig. 3.3. The energy loss of the beam electrons is proportional to the atomic number,  $Z$ , and the distance travelled in the specimen,  $z$ .

### 3. EXPERIMENTAL

---

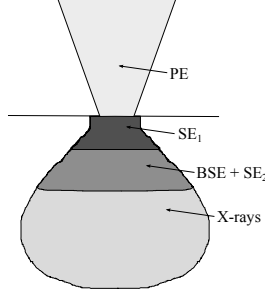


**Figure 3.3:** The volume reached by the primary electrons (PE) and the origin of different signals. Secondary electrons ( $SE_1$ ) generated directly by the PEs that escape the specimen are originating from a small volume close to the surface. Backscattered electrons (BSE) can travel longer distances in the specimen and hence originate from a larger volume. As BSEs travel in the specimen they will create secondary electrons ( $SE_2$ ) contributing to the total SE signal. X-rays can travel even larger distances in the specimen and hence have the largest origin volume.

#### 3.1.4 Beam interaction with carbon nanotubes

For thin specimens of a low atomic number, such as CNTs, the electron beam will penetrate the specimen losing only a negligible amount of energy. Also the probability of backscattering from such specimen is low resulting in a small interaction volume. The majority of the electrons coming from a CNT, as a result of the electron beam, are thus SEs directly generated by the incident beam. In order for these electrons to reach the detector they should not be reabsorbed or scattered in the CNT. The probability of escaping from a specimen decreases with the distance travelled in the solid as:

$$P_{escape} \propto e^{-\alpha z} \quad (3.4)$$

where  $\alpha$  is the absorption coefficient for SE of the specimen material. Assuming the SE generation to be proportional to the thickness ( $t$ ) and using Eq. 3.4, an expression for the SE yield ( $\delta_t$ ) as a function of  $t$ , was derived in [51]:

$$\delta_t \propto \frac{1}{2\alpha} \left( 1 - e^{-\alpha t} (1 - \alpha t) - (\alpha t)^2 \int_{\alpha t}^{\infty} \frac{e^{-\xi}}{\xi} d\xi \right) \quad (3.5)$$

where the  $t$  is a function of the lateral coordinates,  $t = t(r)$ .

The SE yield is also dependent on the tilt angle between the specimen and the electron beam. Defining the tilt angle  $\phi$  as the angle between the surface normal and the beam, the SE yield then depends on  $\phi$  approximately as [52]:

$$\delta_\phi \propto \sec \phi \quad (3.6)$$

where  $\phi$  is a function of the lateral coordinates,  $\phi = \phi(r)$ . For materials with low  $Z$  the dependence of  $\delta_\phi$  on  $\phi$  becomes more rapid. However, the dependence becomes slower for lower acceleration voltages, and Eq. 3.6 is a good approximation for CNTs when using low acceleration voltages. Combining Eq. 3.5 and 3.6 gives the total SE yield:

$$\delta_{sim}(r) = \delta_t(r)\delta_\phi(r) \quad (3.7)$$

From this equation the cross-sectional SE yield coming from a CNT can be modelled by using the dimensions of a CNT. An example of two such SE yields is shown in Fig. 3.4 (a) obtained using two different values of  $\alpha$ . As there are no experimental values of  $\alpha$  for CNTs listed in the literature, we used the absorption coefficient for carbon  $\alpha = 1/20\text{nm}^{-1}$  listed in [53]. The SE yield is fairly insensitive to changes in  $\alpha$ , as is shown in Fig. 3.4 where two  $\delta$ , obtained using different values of  $\alpha$ , are plotted. Having an infinitely sharp electron-probe shape, i.e  $d_p = 0$ , an integrated intensity profile of a CNT from an SEM image would look like Fig. 3.4 (a). But the size of the electron probe is finite and can be described by  $i(r)$ . The resulting SEM image will then be a convolution of  $\delta_{sim}(r)$  with  $i(r)$ :

$$I(r) = [\delta * i](r) = \int \delta(r')i(r - r')dr' \quad (3.8)$$

When imaging details that are large compared to the electron-probe, the convolution would be negligible. For details comparable in size to the electron probe,  $i(r)$  blurs the image significantly. This is illustrated in Fig. 3.4 (b), where  $\delta_{sim}$  has been convoluted with a Gaussian electron-probe shape:

$$i_G(r) = \frac{1}{\sigma\sqrt{2\pi}} \exp\left(-\frac{r^2}{2\sigma^2}\right) \quad (3.9)$$

and with a Lorentzian electron-probe shape:

$$i_L(r) = \frac{1}{\pi} \frac{\frac{1}{2}\Gamma_L}{r^2 + (\frac{1}{2}\Gamma_L)^2} \quad (3.10)$$



### 3. EXPERIMENTAL

A full width at half maximum ( $\Gamma$ ) of 2.1 nm was used for both electron-probe shapes. Where the  $\Gamma_G = 2\sqrt{2\ln 2}\sigma$  and  $\Gamma_L$  is the full width at half maximum for the Gaussian and the Lorentzian distribution respectively. Comparing Fig. 3.4 (a) and (b) it is apparent that the resulting intensity distribution is much smoother than the SE yield. The convolution in Eq. 3.8 was performed in MATLAB where the products of small elements of  $\delta_{sim}(r)$  and  $i(r)$  were added together numerically. The integrations limits were chosen to be  $[R + 5\Gamma, R - 5\Gamma]$  since both  $i_G(r)$  and  $i_L(r)$  quickly go to zero.

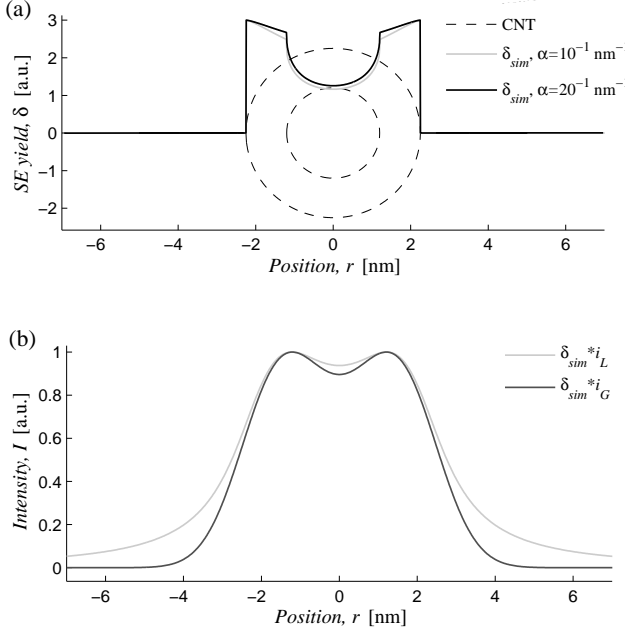


**Figure 3.4:** (a) Plots of the total SE yield, obtained using different values of  $\alpha$ , along with the CNT dimensions used as input. (b) Simulated height normalised intensity profiles obtained using the secondary electron yield in (a).

#### 3.1.4.1 Simulation

The model of how the SEM image is constructed (Eq. 3.7), was tested on SEM images of CNTs. Individual CNTs were first imaged in a JEOL (JEM 2100) TEM equipped with a LaB<sub>6</sub> cathode and a digital camera from Gatan (SC1000 Orsius). The samples consisted of two types of MWCNTs obtained from Nanocyl: NC2100 and NC2101, described in more detail in section 4.2.1. The CNTs were first dispersed in ethanol and then sonicated for 15 min to reduce bundling, thus simplifying imaging of individual CNTs. The suspension was drop-casted onto holey carbon support films for TEM (R 2/1 produced by Quantifoil). In these samples, individual CNTs stuck out over the holes in the carbon film and could be imaged without any underlying substrate. The same individual CNTs were subsequently imaged in a LEO 1530 FEG-SEM using the in-lens detector. The films were mounted in a custom made scanning transmission electron microscopy holder for the SEM. This holder enabled imaging of the same CNTs without any underlying substrate. Before exposing the samples to the electron beam, they were left in the SEM chamber for at least 10 hours, giving an SEM-chamber pressure of about  $5 \times 10^{-7}$  mbar. This was done in order to minimize electron beam-induced deposition (EBID), which can build up amorphous carbon on the CNTs and increase their diameters [54]. To further reduce EBID, the CNTs were only exposed to the beam while imaging and the amount of EBID was later checked by subsequently examining the same CNTs in the TEM. Only negligible amounts of EBID were seen in our samples during the final TEM imaging. Another way of checking the amount of EBID is to look at SEM image sequences and see if the image changes with time, but this is much less accurate than using a TEM.

From the TEM images the inner and outer diameters of the CNTs were obtained and used to get an expression for  $\delta_{sim}$ . Linear combinations of  $i_G(r)$  and  $i_L(r)$  (Eq. 3.9 and 3.10), having the same  $\Gamma$ , were used as  $i_{sim}(r)$  in order to reproduce the integrated intensity profiles of the SEM image. On average it was found that an electron-probe shape consisting of:

$$i_{sim}(r) = 0.5i_G(r) + 0.5i_L(r) \quad (3.11)$$

having  $\Gamma_G = \Gamma_L = 2.05 \pm 0.05$  nm reproduced our SEM images satisfactory. An example of this is shown in Fig. 3.5.

### 3. EXPERIMENTAL

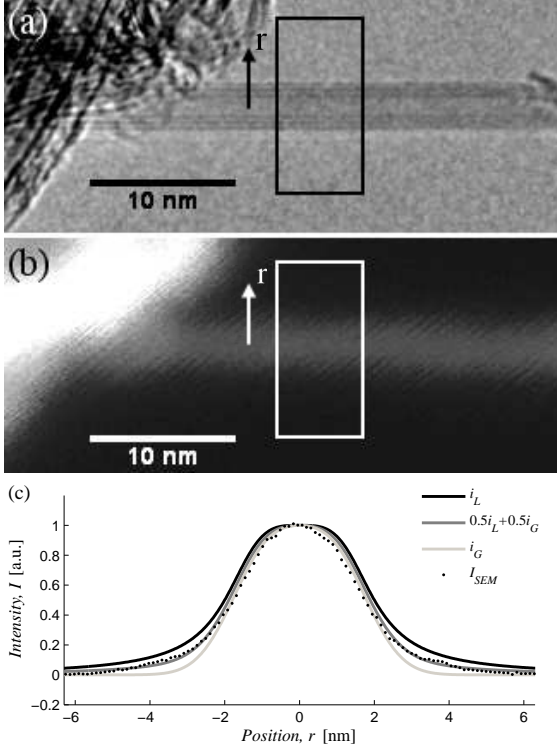


**Figure 3.5:** TEM (a) and SEM (b) image of the same CNT. The boxes in (a) and (b) show the areas from where the integrated intensity profiles were obtained. Along with the integrated intensity profile from the SEM image simulated intensity profiles are plotted in (c), obtained using different  $i(r)$ .

A two dimensional version of Eq. 3.11 was also used to deconvolute SEM images of CNTs, by using it as the input point-spread function in the MATLAB-function `deconvblind`. An image deconvoluted in this way is shown in Fig. 3.6 along with the raw SEM image and a comparison of their intensity profiles. It is apparent from Fig. 3.6 that the image gets sharper and reveals more detail than the raw image, but the deconvoluted intensity profile is still far from the SE yield shown in Fig. 3.4. One reason for this discrepancy is that there is random noise in the raw SEM image. This noise is not related to the electron-probe shape and hence cannot be further resolved by

the deconvolution. In order for a deconvolution to work well,  $i(r)$  has to be accurately described. A method for determining the size of  $i(r)$  have been suggested [55]. However this method assumes a completely Gaussian shaped  $i(r)$  and cannot determine probe sizes smaller than 2 nm.

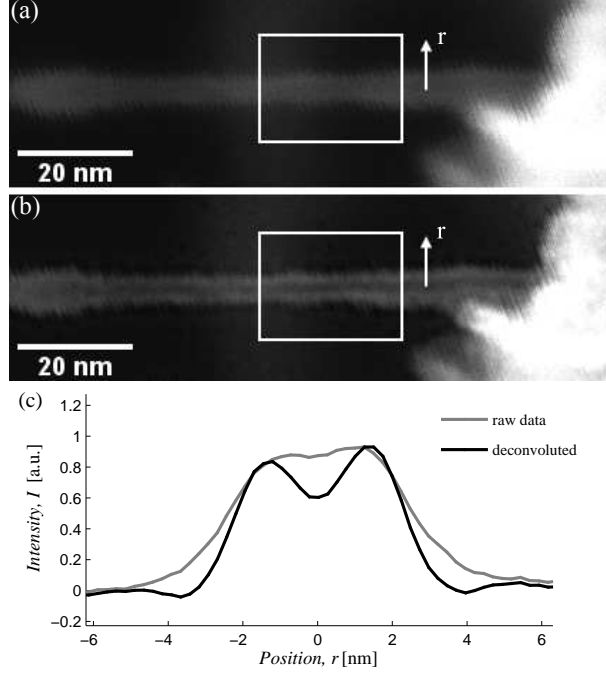


**Figure 3.6:** Raw (a) and deconvoluted (b) SEM images. The integrated intensity profiles from the boxes in (a) and (b) are plotted in (c). The inner diameter is more clearly seen in the deconvoluted image.

Using the model described above to simulate intensity profiles renders a good estimation of  $i(r)$  but requires prior knowledge about the CNT dimensions, in our case obtained from TEM images. Using the image formation mechanisms we developed a method where accurate estimations of the outer CNT diameter can be made without requiring a detailed description of  $i(r)$ . This method uses the distance between the points where the intensity profile's second derivative changes sign (zero points) as the

### 3. EXPERIMENTAL

---

diameter of the CNT. Looking at a convolution of a step function,  $H(r - r_0)$ , and an arbitrary symmetric electron-probe shape  $I_H(r) = [H * i](r)$ , its second derivative changes sign when the maxima of  $i(r)$  meets the edge. However, the SE yield of a CNT is not a step function, but it does have sharp steps at the start and end. Taking the derivative of an intensity profile directly is not possible because of the noise in the image. We therefore fitted a 10th order polynomial to the intensity profile, yielding a smooth enough function to differentiate. It is important that the polynomial fit follows the experimental data and the SEM image should therefore have a high signal-to-noise ratio. We have used the zero points of the polynomial fit to  $\frac{d^2}{dr^2}I(r)$  to estimate the CNT diameter from SEM images,  $d_{SEM}$ , for a number CNTs. These estimations were compared to the diameters measured in TEM images,  $d_{TEM}$ . Good agreement between  $d_{SEM}$  and  $d_{TEM}$  was obtained as is shown in Fig. 3.7 (b). The accuracy of this method was studied by simulating various intensity profiles, using Eq. 3.11 as  $i(r)$  with  $\Gamma = 1 - 3$  nm. The CNT used to obtain  $\delta_{sim}$  had an inner diameter of 1 nm and additional layers were added to get a thicker CNT. The results of these simulations are shown in Fig. 3.7 (c), and one can see that the method estimates the outer diameter accurately for  $\Gamma < d_{outer}$ . When  $\Gamma$  is larger than the outer diameter the method overestimates the outer diameter, but for  $d_{outer} > \Gamma$  it is independent of  $\Gamma$ .

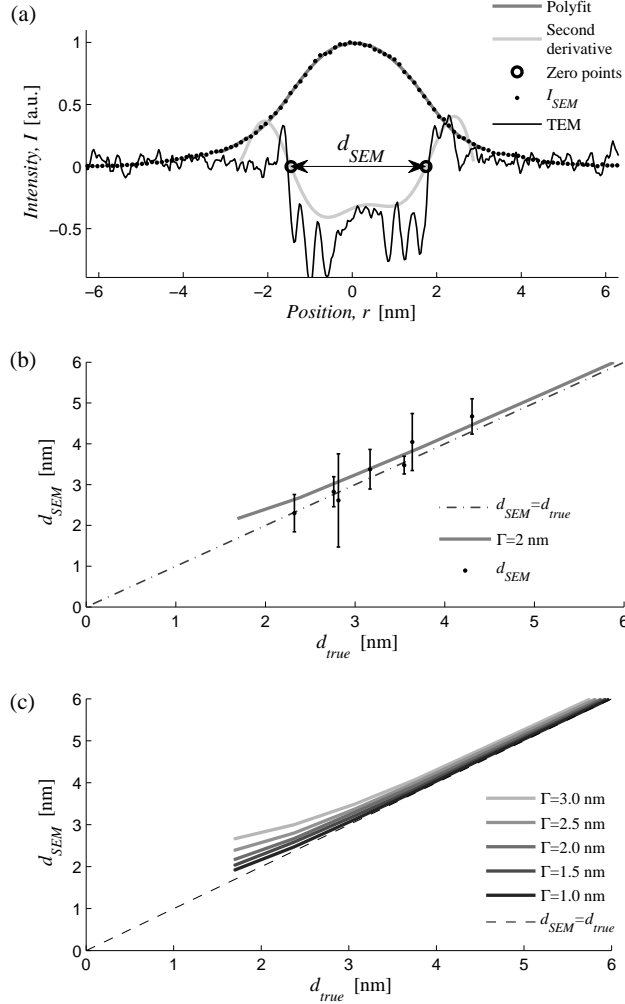


**Figure 3.7:** (a) The TEM and SEM profiles from Fig. 3.5 are shown along with a polynomial fit to the SEM profile and its second derivative. (b) Diameters from the second derivative method versus the diameter obtained from TEM images. Gray line shows the estimated diameter from simulations (using  $\Gamma_G = \Gamma_L = 2$  nm). (c) Estimated diameters versus true diameter for different probe sizes.

### 3. EXPERIMENTAL

---

#### 3.2 In situ SEM-AFM

Measurements of the stiffness of individual CNTs were made using a custom built in situ SEM-AFM controlled by software and electronics from Nanofactory Instruments [56]. The instrument is similar to Nanofactory Instruments in situ TEM-AFM [8]. As shown in Fig. 3.8 the instrument consists of a tip holder attached to a piezoelectric tube and an opposing force sensor. The sample is attached at the end of a metal tip which is fastened to the tip holder. This has six metal springs embracing a sapphire ball that is attached to the piezoelectric tube. By applying sawtooth voltages to the piezoelectric tube, the tip holder will slip against the sapphire ball and can thereby be moved in all three dimensions. This inertial slider mechanism provides coarse motion of the sample in three dimensions, described in more detail in [57]. The sensor is a piezoresistive AFM cantilever, obtained from Nanofactory Instruments, that was micromachined on an n-type silicon on insulator chip [8]. On one face of the cantilever, a shallow ion-implantation of boron was made, creating a piezoresistor that changes resistance when the material is strained. Thus a deflection of the cantilever alters the resistance of the piezoresistor. By including this piezoresistor in a Wheatstone bridge, consisting of another identical dummy piezoresistor and two known resistances, the output bridge-voltage will be proportional to the force exerted on the cantilever.

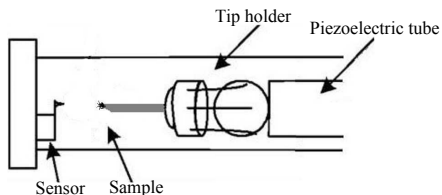


**Figure 3.8:** Schematic sketch of the in situ SEM-AFM instrument. Modified from Fig. 2 in [8] printed with permission from © 2008 IEEE.

##### 3.2.1 Calibrating the in situ SEM-AFM

Calibration of the in situ SEM-AFM requires calibration of the piezoelectric tube movement and the AFM sensor. The motion of the piezoelectric tube was calibrated by applying a voltage to it and measuring the resulting displacement inside the SEM, giving a constant,  $dz/dU$ . The displacements were obtained by measuring the change in

distance between the tip and a static reference surface, as shown in Fig. 3.9 (a)-(c). This was done in small voltage steps, both going forward and backward, in order to account for the piezoelectric creep. Obtained displacements were plotted against the applied voltages and a linear function was fitted to the plotted values, as shown in Fig. 3.9 (d). This was done for a number of runs and the mean value of the obtained slopes was used as the constant  $dz/dU$  in the software controlling the piezoelectric tube.

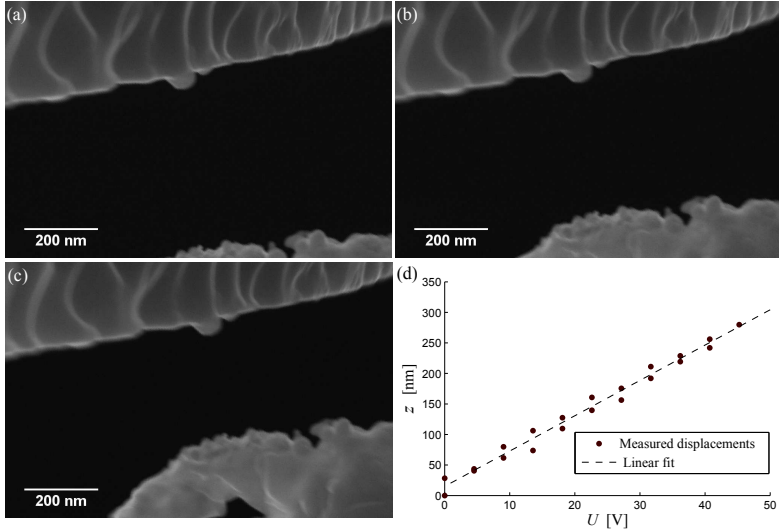


**Figure 3.9:** Voltages were applied to the piezoelectric tube, causing a movement of the tip towards a static reference surface (a)-(c). The change in distance between the cantilever and the reference surface was used to obtain the displacement of the piezoelectric tube at the applied voltage. Plotting these displacements,  $z$ , versus the applied voltages,  $U$ , yields the constant.

Calibration of the AFM sensor requires a calibration of two constants: the piezoresistive constant  $C$  [mV/nm] of the piezoresistor, and the spring constant  $k$  [N/m] of the cantilever. This was done by gluing a reference cantilever to a wire, and mounting this wire in the tip holder. The reference cantilevers (NSC18/F/AIBS/5) were obtained from MikroMasch, and had been calibrated using the plan view dimensions and the resonant frequency of the cantilever in a fluid [58]. By pushing a part of the rigid silicon wafer against the piezoresistive cantilever the piezoresistive constant was calibrated,



### 3. EXPERIMENTAL

---

as shown in Fig. 3.10 (a). This was done by applying a voltage to the piezoelectric tube, displacing the reference cantilever a distance  $\Delta z$ . The wafer, consisting of Si, was assumed to be rigid. Hence the piezoresistive cantilever was also displaced  $\Delta z$ , generating a voltage signal,  $\Delta U$ . This  $\Delta U$  was plotted versus  $\Delta z$  and the mean value of slopes in such graphs were taken as the constant  $C$ .

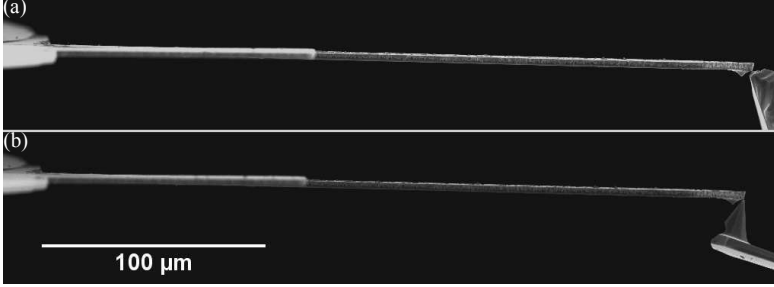


**Figure 3.10:** SEM images taken during (a) calibration of the piezoresistive constant and (b) the spring constant of the sensor cantilever. The calibration was done by pushing a rigid surface in (a) and a reference cantilever in (b) against the sensor cantilever (to the left).

The spring constant of the piezoresistive cantilever was calibrated by pushing the reference cantilever against it, as shown in Fig. 3.10 (b). By applying a displacement  $\Delta z_{\text{applied}}$  to the piezoelectric tube, both the reference cantilever and the sensor cantilever will be deflected through:  $\Delta z_{\text{applied}} = \Delta z_{\text{sensor}} + \Delta z_{\text{reference}}$ . The displacement of the sensor was obtained from the voltage output using the piezoresistive constant  $C$  calibrated in the previous step. Using the relation between the displacements one can derive the relation between the spring constants of the sensor and the reference cantilever:

$$k_{\text{sensor}} = k_{\text{reference}} \left( \frac{\Delta z_{\text{applied}}}{\Delta z_{\text{sensor}}} - 1 \right) \quad (3.12)$$

The ratio  $\frac{\Delta z_{\text{applied}}}{\Delta z_{\text{sensor}}}$  was obtained from the slopes in graphs where  $\Delta z_{\text{sensor}}$  was plotted versus  $\Delta z_{\text{applied}}$ . As the spring constant of the cantilever is highly dependent on its length, or where the force is applied, the reference cantilever was pushed against the outermost part of the sensor, i.e. the same part used in subsequent force measurements.

## Chapter 4

# Materials

### 4.1 Synthesis methods

Literature on the synthesis of tubular carbon structures is abundant and there are several synthesis methods [3, 59], resulting in different structures. In this chapter, only a short description of the most common methods will be presented. These methods are arc discharge, laser ablation, and chemical vapor deposition.

#### 4.1.1 Arc discharge

The MWCNT studied in the paper by Iijima [1] were obtained by putting two graphite electrodes in close proximity, about 1 mm, in a controlled argon atmosphere. Variations of this method have been used in a number of studies where the gas in the atmosphere can be altered as well as the pressure in the chamber. When a voltage is applied between the electrodes a plasma is first formed by the gas. The heat from this plasma vaporizes carbon atoms that become part of the plasma. Ionized carbon atoms are then attracted to the positive electrode where they condensate and form various sorts of carbon, including amorphous carbon, fullerenes, and of course CNTs. The final product thus needs purification steps in order to get a pure CNT sample. By using pure graphite electrodes, only MWCNTs are grown, but by including metal catalysts, e.g. Co, Ni, or Fe in the negative electrode, SWCNTs are grown [12, 13].

CNTs synthesized using this method are straight and needle-like, indicative of high crystalline quality, i.e. a small defect density. One drawback of this method is the small

## 4. MATERIALS

---

production yield of CNTs. Another problem is the high level of by-products that have to be removed, making this method unsuitable for large scale production.

### 4.1.2 Laser ablation

In the laser ablation method, like in the case of arc discharge, CNTs are formed from vaporized graphite. In this method a target, containing of graphite mixed with small amounts of catalytic metals, e.g Ni, Co, or Fe, is exposed to intense laser pulses that vaporizes small amounts of the target per pulse [60]. The target is placed in a heated tube furnace,  $T > 1000^{\circ}\text{C}$ , in which an inert gas is passed. CNTs are formed in the plasma created by the laser and carried from the target by the inert gas towards a cold finger on which they condensate.

CNTs obtained using this method are small in diameter with few walls of high crystalline quality. However the drawback of this method is, as in the case of arc discharge, that it cannot be scaled up to create large amounts of CNTs.

### 4.1.3 Chemical vapor deposition

Chemical vapor deposition (CVD) is different to the two previous methods since it is easily scaled up to produce large amounts of CNTs. In principal this method consists of a volatile gas, containing carbon, that is decomposed, enabling growth of CNTs from catalyst particles [59]. Growth takes place in a chamber, in which the volatile gas is fed along with other gases. The pressure and temperature of the chamber vary for different CVD methods. The catalyst particles can be patterned on a substrate before growth, created by decomposition of volatile gases, or simply fed as particles along with the gas in the chamber. This enables growth from substrate supported catalysts or from floating catalysts.

There are numerous models proposed to elucidate the growth process from a catalyst particle. Most models are based on the vapor-liquid-solid (VLS) mechanism [61] where carbon is absorbed by a liquid catalyst particle that eventually becomes supersaturated, leading to nucleation of carbon. However, no model can predict what happens at the catalyst and no CVD process can yet exactly control the chirality or diameter of the resulting CNTs.

Because of the many variables involved in CVD methods, the resulting structures from different CVD methods vary a lot and can be tailored to yield predominantly

SWCNTs, MWCNTs or even vertically aligned carbon nanofibers (VACNFs). In general the resulting structures are of lower crystalline quality than CNTs obtained from arc discharge and laser ablation. This lower crystalline quality can be seen in TEM-images where CVD-grown tubes are less straight and less needle-like. The walls also have small perturbations that are seldom present in highly crystalline CNTs. The advantage of this method is the feasibility of large scale production, and there are now a number of companies producing large quantities of CVD-grown CNTs.

## 4.2 Materials used

In this thesis two types of materials were used: commercial CVD-grown CNTs and CVD-grown vertically aligned carbon nanofibers (VACNFs).

### 4.2.1 CVD-grown carbon nanotubes

Two types of CNTs were obtained from Nanocyl: NC2100 and NC2101 [62]. Both types were synthesized using a method Nanocyl calls "catalytic carbon vapor deposition". The difference between the two types is that NC2101 had been functionalized with a carboxylic acid group (-COOH) in order to reduce bundling. The amount of -COOH in the samples is however very low, less than 1% [62], so it should not affect the material properties much. Further on in this thesis, the NC2100 and NC2101 types will be referred to as CNT and f-CNT respectively, where f highlights the functionalization.

The powder resulting from the synthesis is purified by Nanocyl, aiming at removing catalyst residues and amorphous carbon. After the purification, the powder is said to contain more than 90% carbon and less than 10% catalyst residues. Nanocyl also states, after imaging in TEM and SEM, that the CNTs are preferentially double-walled and that the average outer diameter and length of the CNTs are 3.5 nm and 1-10  $\mu\text{m}$  respectively. Although the mean values for the diameter is relatively small, our samples studied in TEM and SEM, contained CNTs with diameter larger than 18 nm. The large diameter CNTs often had small inner diameters.

Samples used in the in situ SEM-AFM instrument (described in section 3.2) are attached to a thin metallic wire, thereby requiring some sample preparation. The CNT containing powder was dispersed in ethanol and then sonicated for about 15 min, in order to separate the tubes so that individual ones could be probed. Sonication for

## 4. MATERIALS

---

longer times can cause mechanical damage to the CNTs [63]. CNTs were therefore studied in TEM, showing no signs of mechanical damage after treatment. Sonication of CNTs suspended in chlorinated solvents can, in the presence of Fe nanoparticles, cause doping and disrupt the electronic band structure of the CNTs [64]. This could possibly affect the mechanical properties, and chlorinated solvents were avoided here. Droplets of the CNT-ethanol suspension were placed on a clean glass substrate and allowed to dry, resulting in well separated soot particles with a diameter of about 100  $\mu\text{m}$ . Individual particles were then attached to thin silver wires by first coating the wire tip with conducting epoxy and then picking up particles under an optical microscope, see Fig. 3.8 for experimental set-up.

### 4.2.2 Vertically aligned carbon nanofibers

Growth of the VACNFs was made by a group from Chalmers University of Technology [43]. They used two different settings growing the VACNFs, resulting in two different structures: group A and B. Both settings started with deposition of 12 nm thick Ni catalyst seeds on reactively sputtered TiN film on top of an oxidized silicon chip. The deposition was made using electron-beam lithography. This was followed by 1 hour annealing at 580°C in nitrogen at 6 mbar inside a AIXTRON 2-inch Black Magic reactor, in which the growth later was started. Both groups of VACNFs was grown using a dc plasma, with a power of 40 W, where the electric field, directed perpendicular to the substrate, aligned the fibers vertically from the substrate. Both groups were grown at substrate temperature of 635°C. For group A a chamber pressure of 3.5 mbar and a  $\text{C}_2\text{H}_2/\text{NH}_3$  ratio of 1/4 was used, while a chamber pressure of 8.9 mbar and a  $\text{C}_2\text{H}_2/\text{NH}_3$  ratio of 1/6 was used for group B. The relative amount of carbon-bearing species (e.g C neutrals and C ions) and etchant species (e.g  $\text{H}^+$  and  $\text{N}^+$ ) generated by the plasma is proportional and inversely proportional to the  $\text{C}_2\text{H}_2/\text{NH}_3$  ratio respectively. Increasing this ratio will therefore increase the non-catalytic precipitation of carbon on the sample, leading to a larger deposition rate of amorphous carbon on the nanofiber during growth [43, 65]. This results in a tapered structure, where a thicker layer of amorphous carbon is deposited at the base of the fiber. Because of this, we define a taperedness factor:

$$\alpha = \frac{r_b - r_t}{l} \quad (4.1)$$

where  $r_b$  and  $r_t$  is the radius at the base and tip respectively and  $l$  is the length of the fiber. More details about the growth of these VACNFs can be found in [42, 43].

Previous studies of similar VACNFs found that the core consist of a graphitic cup-stacked structure, shown in Fig. 4.1, where the graphitic planes have an angle  $\theta$  to the fiber axis [65]. The graphitic planes follow the shape of the catalyst particle. Because of the catalyst particle geometry the graphitic planes are less closely packed in the center of the graphitic core, making this part appear hollow-like in TEM-images. A schematic sketch of the VACNF structure along with a TEM-image of a VACNF is shown in Fig. 4.1. From TEM studies we found that  $\theta$  ranged from about  $10^\circ$  to  $30^\circ$ , and that the graphene cups mimic the shape of the catalyst particle.

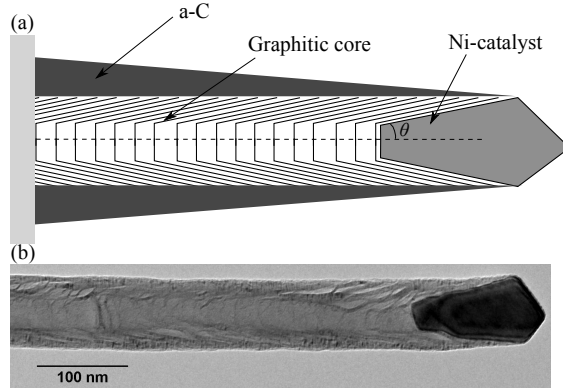


**Figure 4.1:** (a) Schematic sketch of the VACNF structure. (b) TEM-image of the top a VACNF. This VACNF was synthesized using a low  $C_2H_2/NH_3$  ratio, yielding a very small taperdness factor.

In order to perform mechanical measurements on VACNFs, using the in situ SEM-AFM instrument, substrates were glued onto a silver wire using electrical conducting epoxy. In the synthesis process, substrates with the dimensions  $11 \times 2$  mm were used. Using such large substrates makes the tip holder slip against the sapphire ball when moving the sample, due to gravitational forces. Predefined scratches were therefore made on the substrate prior to the synthesis. This facilitated cracking of the substrate so that a smaller piece of the substrate,  $3 \times 2$  mm, could be obtained and glued onto a silver wire. The substrate was positioned so that the VACNFs were parallel to the AFM sensor, facing the sensor in a cantilever-to-cantilever fashion.

#### 4. MATERIALS

---

## Chapter 5

# Mechanical properties

### 5.1 Previous work

#### 5.1.1 Experimental

As discussed in section 2.4.2 CNTs have extraordinary mechanical properties, but because of their small dimensions the characterization of these properties is difficult. This section summarizes different methods that have been used to characterize the mechanical properties of CNTs.

In the earliest article reporting measurements of the Young's modulus,  $E$ , the authors looked at the thermal vibrations and assumed the CNTs to be equivalent to a cantilevered homogeneous cylindrical beam [22]. They showed that the amplitude of the thermal vibrations,  $\sigma$ , of the free end of a cantilevered cylindrical beam is given by:

$$\sigma^2 = \frac{16l^3k_BT}{\pi E(r_o^4 - r_i^4)} \sum_n \beta_n^{-4} \approx 0.4243 \frac{l^3k_BT}{E(r_o^4 - r_i^4)} \quad (5.1)$$

where  $l$ ,  $r_o$ , and  $r_i$  is the length, outer radius and inner radius respectively,  $k_B$  is the Boltzmann constant,  $T$  is the temperature, and  $\beta_n$  is a constant for the free vibration of mode  $n$ . By studying bundles of CNTs in a TEM they found isolated CNTs protruding from the bundle. The amplitude of the vibrations of the free ends was estimated along with the dimensions of the CNTs and used in Eq. 5.1, resulting in  $E = 0.4 - 4.15$  TPa. The big uncertainty stems from the difficulty in determining the amplitude of the vibrations and the length of the CNTs. Another uncertainty is the value of  $T$  which was assumed to be around room temperature, as measured by a thermocouple



## 5. MECHANICAL PROPERTIES

---

close to the sample. The electron beam of the TEM will locally heat up the specimen, thus raising  $T$  of the CNT above room temperature. Using a lower  $T$  than the true will underestimate the value of  $E$  according to Eq. 5.1. The authors estimated the local heating in a later publication to be  $\Delta T = 20 - 40^\circ\text{C}$ , which would shift all their values of  $E$  towards higher values by about 10%. This method, with improved ways for determining  $\sigma$  and  $l$ , has also been used to estimate  $E$  of SWCNT. Assuming the SWCNT to be hollow cylinders with a wall thickness of 0.34 nm a Young's modulus of  $E = 1.25^{+0.45}_{-0.35}$  TPa was found [23].

Another method also assumed CNTs to be cylindrical cantilevers, but instead of looking at their vibrations, individual CNTs were bent with an AFM cantilever [24] (for the geometry see Fig. 5.1 (a)). CNTs were clamped by first depositing CNTs on a  $\text{MoS}_2$  single crystal surface. In the next step pads of a rigid oxide,  $\text{SiO}_2$ , was deposited through a shadow mask. AFM was then used to locate CNTs having a nice geometry and being pinned by a pad. These CNTs were then pushed sideways resulting in  $F$ - $\delta$  curves. Using the slope of this curve, the spring constant,  $k$ , of the CNTs could be determined. Along with the CNT dimensions the Young's modulus could also be determined using the equation from beam theory:

$$E = \frac{4kl^3}{3\pi r_o^4} \quad (5.2)$$

where  $l$  is the length from the point of attachment to the point of the applied force. Using this method an average value of  $E = 1.28 \pm 0.59$  was obtained. Another interesting feature was discovered in the  $F$ - $\delta$  curves, namely a non-linear  $F$ - $\delta$  relation [24]. At a certain deflection the spring constant of the CNT drastically decreased but continued to be linear (or close to). Bumps on the CNTs could be imaged on severely bent CNTs suggesting that the CNTs had buckled, thus causing the change in spring constant. These images were acquired by using a high-friction surface, keeping the CNT bent after it was released by the AFM-tip. Relaxing these CNTs and imaging them again showed no signs of irreversible deformation. Also their  $F$ - $\delta$  behaviour was unaltered after the buckling suggesting this phenomena to be reversible. Other AFM studies have also shown that CNTs can withstand large bending curvatures reversibly [66, 67].

This behaviour was also seen in a TEM study where static and dynamic mechanical deflections were electrically induced in cantilevered MWCNTs [4]. This was done by first attaching carbon soot containing MWCNTs to a fine gold wire. The wire was then

mounted on a piezoelectrically driven translation stage, enabling fine movement of the sample. A potential could also be applied to the sample, and in close proximity, 5-20  $\mu\text{m}$ , a counter electrode was placed. When a potential was applied between the stage and the counter electrode the CNTs became electrically charged and were attracted to the counter electrode. By studying the bending of the CNTs, the charge appeared to be localized at the tip of the CNTs. When applying a time-dependent potential between the stage and the counter electrode, the CNTs began to oscillate. By varying the frequency of the time-dependent potential the eigenfrequency of the CNTs could be obtained. From beam theory it is known that the eigenfrequency of mode  $n$  of a cantilevered cylindrical beam is given by:

$$\nu_n = \frac{\beta_n^2}{8\pi} \frac{1}{l^2} \sqrt{d_o^2 - d_i^2} \sqrt{\frac{E}{\rho}} \quad (5.3)$$

where  $\beta_n$  is the constant for the free vibration of mode  $n$ ,  $l$  is the length of the beam,  $d_o$  and  $d_i$  is the outer- and inner-diameter respectively,  $E$  the Young's modulus, and  $\rho$  is the density. By finding the eigenfrequency of the first mode,  $\nu_1$ , and using  $\beta_1 = 1.875$  along with the CNT dimensions,  $E$  could be extracted. Using this method the authors found values for Young's modulus varying between 1.3-0.1 TPa, where  $E$  seemed to decrease with increasing diameter. The authors explained this decrease with the emergence of another bending mode, which appears in CNTs bent at large curvatures. On the contracted part of the bent CNT a wavelike pattern of ripples was clearly seen in their TEM images. Another work also showed TEM images of this rippling pattern, where MWCNTs embedded in a polymer were studied. MWCNTs bent to high curvatures by the polymer matrix showed that the rippling pattern extended over large regions without any collapse of the MWCNTs [68].

AFM measurements were used in another study where droplets of a suspension containing CNTs were deposited on a well-polished alumina ultrafiltration membrane [49]. This membrane had pores with a diameter of  $\sim 200$  nm. AFM was then used to find CNTs with part of its length lying across a pore, but with most of its length being in contact with the membrane surface. CNTs fulfilling this were strongly attached to the membrane surface and the part lying across a pore was assumed to be similar to suspended beams with circular cross-sections, see Fig. 5.1 (b) for the geometry.

## 5. MECHANICAL PROPERTIES

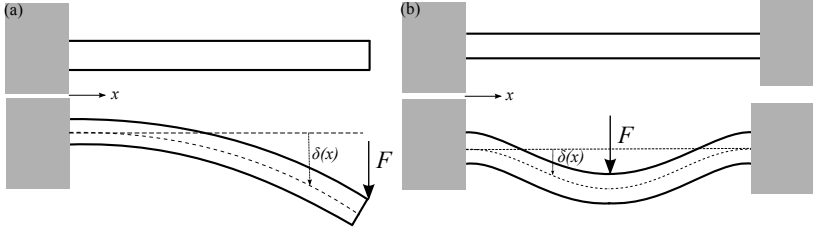


**Figure 5.1:** (a) Cantilevered beam and (b) suspended beam exposed to a point load,  $F$ . From beam theory, the deflection,  $\delta(x)$ , of the beam can be found. The magnitude of  $\delta$  depends on the  $E$  and the dimensions of the beam.

By deflecting the CNT by a distance  $\delta$  with the AFM cantilever at half of the suspended length while measuring the resulting force,  $F$ , the Young's modulus was obtained using the  $F$ - $\delta$  relation from beam theory:

$$\delta = \frac{Fl^3}{3\pi E(d_o^4 - d_i^4)} \quad (5.4)$$

In their work the authors studied three different sorts of MWCNTs: arc-discharge grown, annealed arc-discharge grown, and catalytic chemical vapour deposition (CCVD) grown. The annealed arc-discharge grown MWCNTs were heated to 2500°C, aiming at reducing point defects. Structure disorder is known to be present in a larger extent in CCVD grown tubes, which is why these tubes were used. The study showed no apparent effect of the annealing, since the annealed arc-discharge grown tubes actually had a smaller mean Young's modulus ( $E_{annealed} = 755$  GPa compared to  $E_{as-grown} = 870$  GPa), while  $E$  for CCVD grown tubes was almost two orders of magnitude smaller with a mean value of  $E_{CCVD} = 27$  GPa. The authors explained the small values of  $E_{CCVD}$  with the structure disorder in the CCVD grown tubes, where this disorder made the walls of the MWCNT non-parallel to the tube axis. The structure of these tubes can be approximated with the cup-stacked structure, seen in Fig. 5.2 (a), where cups of graphene are stacked in one another.

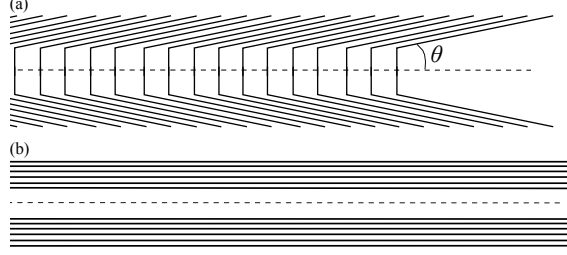


**Figure 5.2:** (a) Cup-stacked structure in comparison with (b) the concentric cylinder structure.

Deviation of the angle  $\theta$  from  $0^\circ$  enables gliding between the planes, and the shear modulus of the MWCNT begin to dominate the deformation. Having such a structure  $E$  would be given by the relation [49]:

$$\frac{1}{E} = s_{11}(1 - \gamma^2)^2 + s_{33}\gamma^4 + (2s_{13} + s_{44})\gamma^2(1 - \gamma^2) \quad (5.5)$$

where  $\gamma = \sin \theta$  and  $s_{ij}$  are the elastic compliances of the material. In graphite  $s_{44}$  is much bigger than the other elastic compliances, significantly lowering  $E$  as soon as  $\theta$  deviates from zero. The dependence of  $E$  on  $\theta$  according to Eq. 5.5 is plotted in Fig. 5.3, where the elastic compliances of graphite  $s_{11} = 0.98 \text{ TPa}^{-1}$ ,  $s_{33} = 27.5 \text{ TPa}^{-1}$ ,  $s_{13} = -0.33 \text{ TPa}^{-1}$ ,  $s_{44} = 240 \text{ TPa}^{-1}$  was used [20]. From Fig. 5.3 it is clear that the Young's modulus drops dramatically even for small  $\theta$ .

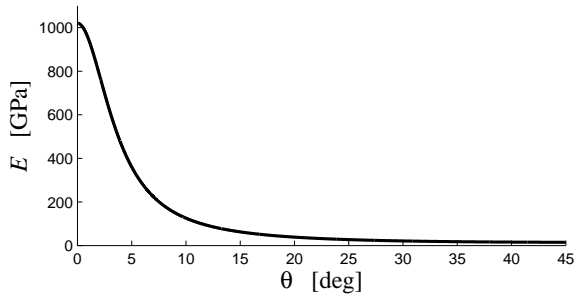


**Figure 5.3:** Dependence of Young's modulus on the angle of the graphene planes, according to Eq. 5.5.

## 5. MECHANICAL PROPERTIES

---

In similar studies the same group later reported low values of Young's modulus ( $10 < E < 100$ ) for CVD grown CNTs appearing to have concentric cylinder structure [69, 70]. They explain the low values of  $E$  with the introduction of structural defects during growth. The exact role and mechanics of these defects are unknown but the authors propose a model of a series of high-quality segments joined by poorly connected nodes [70].

### 5.1.2 Theoretical

Because of the difficulties in controlling and measuring the boundary conditions, the forces, and the displacements of CNTs experimentally, most studies trying to characterize the non-linear behaviour of CNTs have been performed theoretically. The earliest report used molecular dynamics (MD) to model buckling of SWCNTs and DWCNTs [26]. A similar study also used MD, and compared the results to a continuum shell model [27]. They found good agreement between the continuum approach and the MD simulations, and proposed the use of an extended continuum model to study multi-walled tubes. Using MD to study MWCNTs becomes very computationally expensive as the number of walls is increased. Therefore other approaches are also used to model deformation behaviours of MWCNTs.

A refined version of the continuum approach was developed where each individual tube in a MWCNT was modelled as an elastic shell. Each shell was given an effective thickness,  $h$ , an effective Young's modulus,  $E_{eff}$ , and a Poisson's ratio,  $\nu$ , similar to the ones described in [27]. From these properties the flexural rigidity,  $D$ , and the in-plane stiffness,  $C$ , of a shell can be calculated using:

$$D = \frac{E_{eff}h^3}{12(1-\nu^2)} \quad (5.6)$$

and

$$C = E_{eff}h \quad (5.7)$$

In addition, each shell was ascribed with an excess internal strain energy, because of the curvature of the tube, assumed to depend on the diameter as  $1/d^2$ . The wall spacing was set to 0.34 nm, and the van der Waals interactions between the walls was modelled with a Lennard-Jones potential while the shear was assumed to be zero. Using this model, FEM simulations showed a rippling pattern similar to the patterns

observed experimentally [4, 24, 25, 71] in bent tubes. They also found that the moment-curvature,  $M - \kappa$ , dependence was initially linear but changed at the rippling onset. After the rippling onset the  $M - \kappa$  relation is non-linear as the rippling spreads to the inner tubes. When all tubes are rippled the  $M - \kappa$  relation continues to be linear albeit with a smaller spring constant than prior to the rippling.

Modelling the graphene walls as elastic shells works well at small deformations. However, after the rippling onset the graphene walls are largely deformed and the walls will deform non-linearly, the linear shell model then has difficulties in describing this behaviour. Ultimately the simulations should be done using MD, where contributions from each atom are used to determine the behaviour of the MWCNT, but this becomes too computationally expensive. To account for the non-linear mechanical behaviour of the graphene walls one research group used the Green strain tensor to describe the mechanical properties [72]. However their use of the Green strain sensor only permitted them to use flat atomic layers, whereby they modelled the MWCNT as a rectangular beam with the graphite planes being parallel to the axis and perpendicular to the bending plane. Modelling this structure under pure bending using FEM, the authors found a  $M - \kappa$  behaviour they fitted to a bi-linear relation. They also found that the spring constant decreased by a factor of 2, after the rippling onset, and that it starts to ripple at a critical strain of  $\varepsilon_{cr} = 0.006$ .

In another approach [73] the mechanical properties of the graphene walls were systematically inherited from the Brenner atomistic potential. This potential is ascribed to 2D objects in a FEM simulations, thereby not requiring any artificial thickness of the layers. Inheriting the atomic potential includes the non-linear mechanical properties of graphene into the model without increasing the degrees of freedom too much, enabling simulations of thick MWCNTs. This potential also includes the internal strain energy of the walls depending on the diameter as  $1/d^2$ . The inter-wall van der Waals interaction was modelled using a Lennard-Jones potential. Using this model the authors modelled MWCNTs exposed to pure bending and twisting and found the rippling patterns for both loading conditions. In bending they initially found a linear  $M - \kappa$  relation and after the rippling onset the relation followed  $M \propto \kappa^n$  with  $0 < n < 1$ . The critical strain for the rippling onset was found to depend on the outer radius of the MWCNT as  $\varepsilon_{cr} = 0.1/r$ . This contradicts the result of [72], where a constant  $\varepsilon_{cr}$  was predicted.

## 5. MECHANICAL PROPERTIES

---

A similar dependence of  $\varepsilon_{cr}$  on  $r$ , as in [73], was found by a group using MD to simulate the mechanical behaviour of MWCNT [74]. By only using armchair type CNTs they could employ periodic boundary conditions and thereby reduce the number of atoms used in their model to less than 1920. Using only armchair CNTs is a reasonable assumption since earlier reports have shown that the mechanical properties are insensitive to the chirality. The authors used the Tersoff and the Lennard-Jones potential to model the intra-tube and inter-tube interactions respectively. They found that the critical strain depends on the radius as  $\varepsilon_{cr} = 0.05/r$ , i.e. a similar dependence as in [73]. They also found a nearly linear post-rippling  $M - \kappa$  relation albeit with a lower spring constant after the rippling onset. The ratio between the spring constants after and before rippling,  $k_r/k_i$ , was found to depend on the number of walls ranging from 0.15 and converging to 0.65 for MWCNTs with more walls.

All the models discussed above assumed perfect MWCNT with no defects. In a recent study, the model [73] was extended so that the influence of different defects on the mechanical properties was studied [75]. In addition to the intra-plane inherited Brenner potential and the inter-plane Lennard-Jones potential,  $sp^3$  and  $sp^2$  defects between the layers were modelled as tensional and shear spring constants. Using a defect density,  $\rho$ , the authors homogenized the potential energy of these defects, thereby enabling a continuum description. The  $sp^3$  defects were modelled as interstitial carbon atoms linking two adjacent walls together, while the  $sp^2$  defects were modelled as single-atom vacancies in adjacent walls forming a bond. When performing pure bending simulations on identical MWCNTs with varying defect densities the authors found that  $\varepsilon_{cr}$  increased linearly with  $\rho$ . They also found that the post-rippling stiffness increased linearly with  $\rho$  for  $sp^3$  defects and close to linearly for  $sp^2$  defects. However the introduction of  $sp^2$  defects also lowered the pre-rippling stiffness, while it was unaffected for the  $sp^3$  defects.

## 5.2 In situ SEM-AFM bending experiments

### 5.2.1 Multi-walled carbon nanotubes

Sample preparation was described in section 4.2.1, where soot particles containing CNTs were attached to a silver tip using electrically conductive epoxy. This tip was then mounted in the in situ AFM instrument described in section 3.2, enabling 3D

motion of the sample. To be able to locate suitable CNTs and measure their dimensions, the in situ AFM instrument was mounted inside an SEM. Straight tubes with no visible defects or amorphous carbon on them and attached so that they were parallel to the AFM cantilever, were located and brought in contact with the AFM cantilever. This setup is analogous to the cantilever-to-cantilever setup used when calibrating the AFM cantilever, described in section 3.2.1, with the difference that the CNTs are significantly smaller than the AFM cantilever. Overview images of the setup inside the SEM are shown in Fig. 5.4.

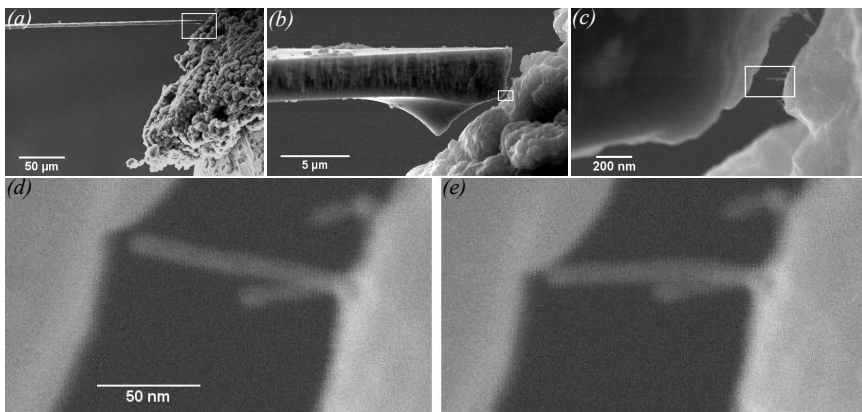


**Figure 5.4:** (a)-(e) show SEM-images of the experimental set-up at different magnifications. In (a) the AFM cantilever and the soot particle are clearly visible. (b) is a magnification of the AFM tip and (c) shows a CNT close to the AFM cantilever. In (d) and (e) the CNT shown in (c) is pushed against the AFM cantilever.

From the SEM images, the radius,  $r$ , and the length,  $l$ , of the CNT can be obtained. The length was estimated by measuring the displacement of the CNT as a function of the distance from the point of the applied force,  $\delta(x)$ , see Fig. 5.5. Using the method of least squares with  $l$  as the fitting parameter, the function of a bent cantilevered beam was fitted to the measured displacements. From beam theory the displacement of a cantilevered beam subjected to a point force at the free end is given by:

$$\delta\left(\frac{x}{l}\right) = \frac{\delta_0}{2} \left( \left(\frac{x}{l}\right)^3 - 3\left(\frac{x}{l}\right) + 2 \right) \quad (5.8)$$

where  $\delta_0$  is the displacement at  $x = 0$ .



## 5. MECHANICAL PROPERTIES

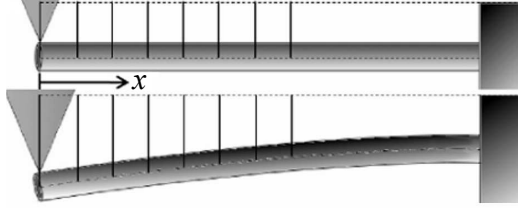


**Figure 5.5:** A schematic showing how the length of the CNTs was determined. Vertical distances was measured from a line drawn from a fixed point on the sample for an unloaded (top) and for a bent CNT (bottom). The difference between these distances gives the deflection of the CNT as a function of  $x$ ,  $\delta(x)$ .

It was found, by comparing TEM- and SEM-images of the same CNT, that the diameter could be estimated by taking the FWHM of a Gaussian function fitted to the SEM intensity profile. This was examined more thoroughly, and it was found that a more accurate method is to fit a high order polynomial to the intensity profile and finding the second derivative zero points of this fit. The distance between these points gives the diameter of the CNT. This method is described in section 3.1.4 and in Paper II.

Pushing the CNTs against the cantilever gives  $F$ - $\delta$  curves, where the force detected by the cantilever is plotted versus the piezo-displacement. An example of a  $F$ - $\delta$  curve is seen in Fig. 5.6.

As can be seen in Fig. 5.6 the spring constant abruptly changes at a certain critical displacement  $\delta_{cr}^{piezo}$ . The critical displacement of the CNT,  $\delta_{cr}^{CNT}$ , is related to the critical displacement of the piezo through:

$$\delta_{cr}^{CNT} = \delta_{cr}^{piezo} \left( 1 - \frac{k^{tot}}{k^{cant}} \right) \quad (5.9)$$

where  $k^{tot}$  and  $k^{cant}$  is the spring constant obtained from the  $F$ - $\delta$  and the spring constant of the cantilever respectively. Using  $\delta_{cr}^{CNT}$  and assuming the CNT to be equivalent to a cantilevered beam with circular cross-section, the maximum critical strain can be calculated using:

$$\varepsilon_{cr} = \frac{3\delta_{cr}^{CNT}r}{l^2} \quad (5.10)$$

where  $r$  and  $l$  is the radius and length of the CNT respectively.

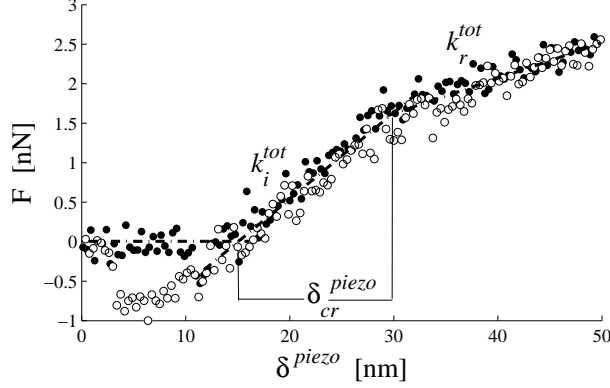


**Figure 5.6:**  $F$ - $\delta$  curve obtained by pushing an cantilevered individual CNT. Black dots are from forward motion and hollow dots are from moving backwards. At a critical displacement the spring constant of the CNT drastically changes. This change is reversible since the force response is identical when moving backwards.

Other useful parameters from the  $F$ - $\delta$  curve are the spring constants  $k_i^{tot}$  and  $k_r^{tot}$ . These are related to the spring constant of the CNTs,  $k^{CNT}$ , through:

$$k^{CNT} = \frac{k^{cant} k^{tot}}{k^{cant} - k^{tot}} \quad (5.11)$$

where  $k^{cant}$  is the spring constant of the cantilever. Using  $k_i^{CNT}$  and assuming the CNTs to be equivalent to cantilevered beam with a circular cross-section with inner and outer radius  $r_i$  and  $r_o$  respectively, the Young's modulus can be calculated using:

$$E = \frac{4k_i^{CNT} l^3}{3\pi r_o^4} \times \frac{r_o^4}{r_o^4 - r_i^4} \quad (5.12)$$

There is no way of measuring very small  $r_i$  using SEM, but the factor  $r_o^4/(r_o^4 - r_i^4)$  quickly goes to 1 as the ratio  $r_i/r_o$  decreases. When studying CNTs from the same batch in a TEM it was found that most CNTs had  $r_i/r_o \leq 0.5$  resulting in  $r_o^4/(r_o^4 - r_i^4) \leq 1.07$ , hence the factor  $r_o^4/(r_o^4 - r_i^4)$  in Eq. 5.12 can be neglected.

As discussed previously two theoretical studies predicted a dependence of  $\varepsilon_{cr}$  on the outer radius of the CNT [73, 74], while another predicted a constant  $\varepsilon_{cr}$  [72]. We therefore plotted the values of  $\varepsilon_{cr}$  versus  $r$  along with these theoretical predictions, and the result is shown in Fig. 5.7.

## 5. MECHANICAL PROPERTIES

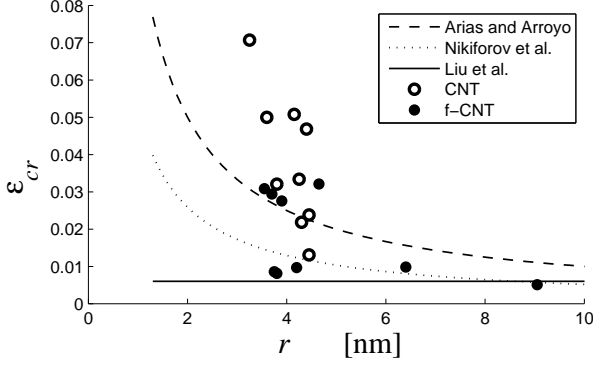


**Figure 5.7:** Critical strain,  $\varepsilon_{cr}$ , plotted versus the radius,  $r$ , along with three theoretical predictions: Arias and Arroyo [73], Nikiforov et al. [74], and Liu et al. [72].

There have been reports suggesting a radial dependence of  $E$  and explaining this with the emergence of the rippling mode [4]. Using only the initial spring constant before the CNT begin to behave non-linear,  $k_i^{CNT}$ , as in Eq. 5.12, this excludes the effect on the rippling mode. We therefore plotted the values of  $E$  versus  $r$  to investigate if the values of  $E$  depended on  $r$ , and the result is shown in Fig. 5.8.

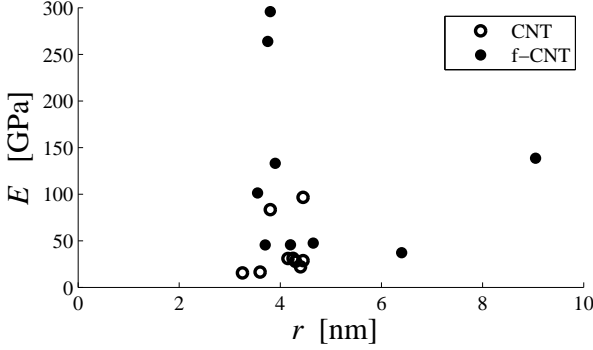


**Figure 5.8:** Young's modulus plotted versus the radius,  $r$ .

As can be seen in Fig. 5.7 there is a large variation in the values for  $\varepsilon_{cr}$  for CNTs with similar radii. Theoretical work has suggested that  $\varepsilon_{cr}$  increases with increasing defect density [75]. Two single-atom vacancies in neighbouring layers can together form an inter-wall bridge. This was modelled using a shear spring constant and a normal spring constant, resulting in a stronger inter-wall interaction. With a stronger inter-wall interaction, the MWCNT acts more like a solid cylinder instead of individual shells and the critical strain thereby approaches that of a solid cylinder. We have therefore plotted our obtained values of  $E$  versus  $\varepsilon_{cr}$  and the result is shown in Fig. 5.9. There is a trend for tubes with low  $E$  to be more resistant to rippling (large  $\varepsilon_{cr}$ ), consistent with the results in [75]. The large variation of  $E$  for similar radii shown in Fig. 5.8 likely related to the fact that these are CCVD grown tubes. Similar variations have previously been observed for CCVD grown MWCNTs, where the authors explained the large variation with defects being introduced in the growth process [70]. We also found that tubes having a large  $E$  rippled at lower  $\varepsilon_{cr}$  than tubes having lower  $E$ . Ultimately one would like to have tubes that are resistant to rippling while retaining a high stiffness.

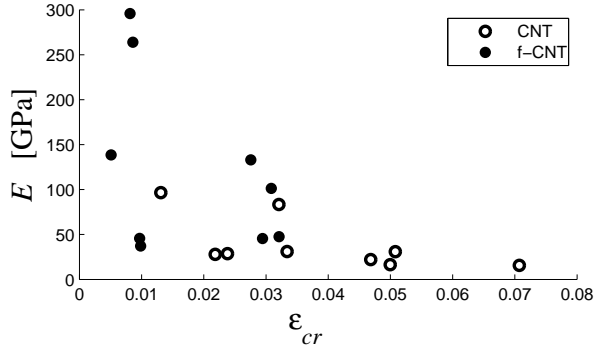


**Figure 5.9:** Young's modulus plotted versus the critical strain,  $\varepsilon_{cr}$ .

### 5.2.2 Vertically aligned carbon nanofibers

In order to perform mechanical measurements on VACNFs, a substrate containing VACNFs (described in section 4.2.2) was cut and glued onto a silver wire. This wire

## 5. MECHANICAL PROPERTIES

was mounted in a tip holder which was inserted in the in situ SEM-AFM instrument, see Fig. 3.8 for experimental set-up.

Force curves from 5 fibers of group A and 6 fibers of group B were obtained. SEM images of an unloaded and bent CNF, along with a  $F$ - $\delta$  curve, are shown in Fig. 5.10.

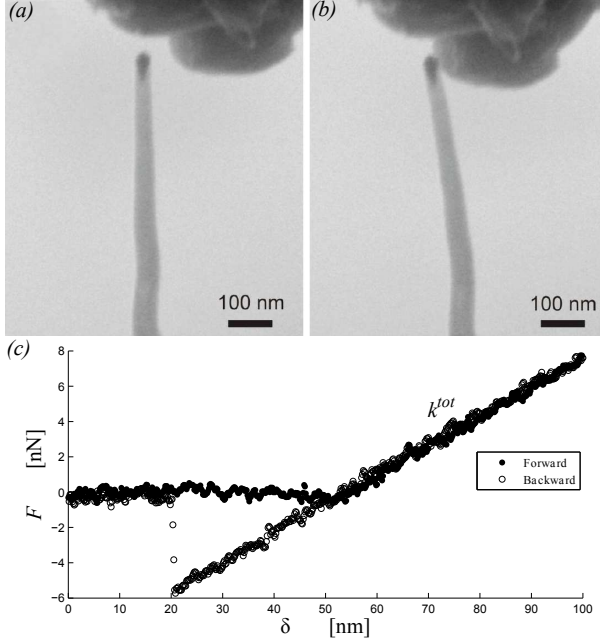


**Figure 5.10:** SEM image of a CNF (a) before bending and (b) bent. (c)  $F$  -  $\delta$  curve obtained by pushing an individual CNF.

From these  $F$ - $\delta$  curves the spring constants of the fibers,  $k^{CNF}$ , could be obtained from Eq. 5.11 and used to calculate  $E$  of the fibers. Since the fibers were tapered, their area moment of inertia,  $I$ , varied across their length as:

$$I = \frac{\pi (r_t + \alpha x)^4}{4} \quad (5.13)$$

where  $x$  is defined from Fig. 5.5,  $r_t$  is the radius at the tip, and  $\alpha$  is the taperdness factor defined in Eq. 4.1. From beam theory one can deduce that the deflection,  $\delta$ , of

## 5.2 In situ SEM-AFM bending experiments

an elastic beam subjected to a point force,  $F$ , at one end is related to  $F$  as:

$$\frac{d^2\delta}{dx^2} = \frac{4F}{\pi E} \frac{x}{(r_t + \alpha x)^4} \quad (5.14)$$

Integrating Eq. 5.14 twice and using the boundary conditions of a cantilevered beam ( $\delta(l) = \delta'(l) = 0$ ), the relation between the deflection at the point of the applied force can be written as:

$$\delta(0) = \frac{4Fl^3}{3\pi E r_t r_b^3} \quad (5.15)$$

where  $l$  is the length, and  $r_b$  and  $r_t$  is the radius at the base and tip respectively. Using Eq. 5.15 along with  $k^{CNF} = \Delta F / \Delta \delta$ ,  $E$  can be obtained. This was done for the measured fibers and the result is shown in Fig. 5.11, where  $E$  was plotted against the taperedness factor  $\alpha$ .

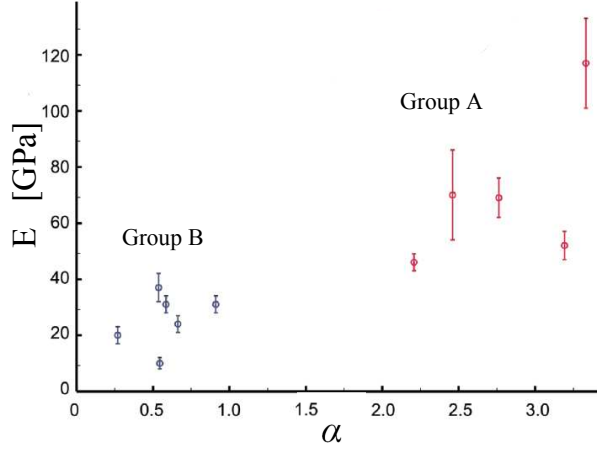


**Figure 5.11:** Young's modulus plotted versus the taperedness factor  $\alpha$ .

As seen in Fig. 5.11  $E$  increases with increasing taperedness. Since the taperedness is created by deposition of amorphous carbon on the fibers during growth, more tapered fibers have more amorphous carbon deposited on them. Modelling the fibers as a homogeneous material (as was done in Eq. 5.14 and 5.15) thus yield a taperedness dependence on  $E$ , since the graphitic core and the amorphous carbon have different elastic moduli. By instead prescribing an Young's modulus of  $E_{core}$  and  $E_{a-C}$  to the

## 5. MECHANICAL PROPERTIES

graphitic core and the deposit of amorphous carbon respectively Eq. 5.14 is rewritten as:

$$\frac{d^2\delta}{dx^2} = \frac{4F}{\pi} \frac{x}{E_{a-C} \left[ (r_t + \alpha x)^4 - r_t^4 \right] + E_{core} r_t^4} \quad (5.16)$$

Integrating this equation twice and again using the boundary conditions of a cantilevered beam, the spring constant of the fiber can be expressed as:

$$k^{CNF} = \frac{\pi \alpha^3 \beta^3 E_{a-C} r_t}{2(\beta^2 - 1) \arctan\left(\frac{\beta(r_b - r_t)}{\beta^2 r_t + r_b}\right) + (\beta^2 + 1) \ln\left(\frac{(1+\beta)(r_b - \beta r_t)}{(1-\beta)(r_b + \beta r_t)}\right) + 2\beta \ln\left(\frac{(1-\beta^2)(r_b^2 + \beta^2 r_t^2)}{(1+\beta^2)(r_b^2 - \beta^2 r_t^2)}\right)} \quad (5.17)$$

where  $\beta = (E_{a-C} - E_{core})/E_{a-C}$ . The method of least squares was used, with  $E_{a-C}$  and  $E_{core}$  as fitting parameters, to fit Eq. 5.17 to our measured values of  $k^{CNF}$ . The result of this fit is shown in Fig. 5.12.

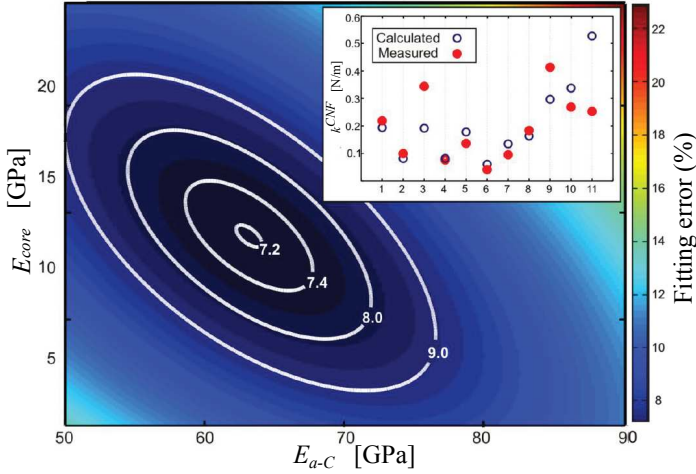


**Figure 5.12:** The mean square difference between the measured spring constants and the spring constants calculated using Eq. 5.17 with  $E_{a-C}$  and  $E_{core}$ . The inset shows the measured values of  $k^{CNF}$  along with calculated  $k$ -values using  $E_{a-C} = 63$  GPa and  $E_{core} = 11$  GPa (the pair of  $E_{a-C}$  and  $E_{core}$  yielding the smallest fitting error) for all 11 measured fibers.

The best fit of Eq. 5.17 to our measured values of  $k^{CNF}$  was obtained using  $E_{a-C} = 63 \pm 14$  GPa and  $E_{core} = 11 \pm 8$  GPa, where the error margins was chosen so that the

## 5.2 In situ SEM-AFM bending experiments

---

fitting error is less than 9%. The low value of  $E_{core} = 11 \pm 8$  GPa, compared to the  $E = 1$  TPa for perfect CNTs, is not surprising since the core consist of a graphitic cup-stacked structure, making the angle between the graphitic planes and the tube axis,  $\theta$ , non-zero. Hence, the graphitic layers will shear against each other when bending the fiber. For graphitic materials the shear modulus is much lower that the in-plane modulus [20]. Thereby, as  $\theta$  grows the shear modulus will govern the mechanical behaviour, according to Eq. 5.5 and shown in Fig. 5.3, and the stiffness in the axial direction will be significantly lowered.



## 5. MECHANICAL PROPERTIES

---

## Acknowledgements

First I would like to thank my supervisor Krister Svensson for giving me the opportunity to pursue my career as a PhD student. You have always found the time to help me when I have ran into difficulties and your passion for physics has been inspiring. I am also grateful to my second supervisor Pavel Krakhmalev for having the patience to read through and give comments on, what has sometimes felt like, endless versions of our manuscripts.

I also would like to thank Farzan Ghavanini and Peter Enoksson at the Chalmers University of Technology for synthesising the VACNF samples, without your contribution there would obviously not have been a project.

I am also thankful to my office neighbours and PhD student colleagues Ana Sofia Anselmo, Leif Ericsson, and Joakim Hirvonen Grytzelius for helping me with teaching and how various instruments work. I also would like to thank my friend Johanna Rosenlind for her support in many situations. Thanks also to all the people, presently and formerly, at the department of physics and electrical engineering for making every day at work enjoyable.

Finally I would like to thank my family and friends for helping me relax from my studies and sustain contact with the world outside the university.



# References

- [1] Iijima, S. *Nature* **354**, 56–58 (1991).
- [2] Monthieux, M. and Kuznetsov, V. *Carbon* **44**, 1621–1623 (2006).
- [3] Dresselhaus, M. S., Dresselhaus, G., and Avouris, P. *Carbon Nanotubes: Synthesis, Structure, Properties and Applications*, Springer, Berlin (2001).
- [4] Poncharal, P., Wang, Z. L., Ugarte, D., and de Heer, W. A. *Science* **283**(5), 1513–1516 (1999).
- [5] Demczyk, B. G., Wang, Y. M., Cumings, J., Hetman, M., Han, W., Zettl, A., and Ritchie, R. O. *Materials Science and Engineering A* **334**, 173–178 (2002).
- [6] <http://www.amroy.fi/partners.php>, (2012-04-27).
- [7] Arroyo, M. and Arias, I. *Journal of the Mechanics and Physics of Solids* **56**, 1224–1244 (2008).
- [8] Nafari, A., Karlen, D., Rusu, C., Svensson, K., Olin, H., and Enoksson, P. *Journal of Microelectromechanical Systems* **17**(2), 328–333 (2008).
- [9] Nafari, A., Angenete, J., Svensson, K., Sanz-Velasco, A., and Olin, H. In *Scanning Probe Microscopy in Nanoscience and Nanotechnology, Volume 2*, Bhushan, B., editor, chapter 3, 59–99. Springer, Berlin (2010).
- [10] Radushkevich, L. and Lukyanovich, V. *Zurn. Fisic. Chim.* **26**, 88–95 (1952).
- [11] Kroto, H. W., Heath, J. R., O’Brien, S. C., Curl, R. F., and Smalley, R. E. *Nature* **318**, 162–163 (1985).
- [12] Iijima, S. and Ichihashi, T. *Nature* **363**, 603–605 (1993).
- [13] Bethune, D. S., Klang, C. H., de Vries, M. S., Gorman, G., Savoy, R., Vazquez, J., and Beyers, R. *Nature* **363**, 605–607 (1993).
- [14] Novoselov, K. S., Geim, A. K., Morozov, S. V., Jiang, D., Zhang, Y., Dubonos, S. V., Grigorieva, I. V., and Firsov, A. A. *Science* **306**, 666–669 (2004).
- [15] Saito, R., Fujita, M., Dresselhaus, G., and Dresselhaus, M. S. *Applied Physics Letters* **60**(18), 2204–2206 (1992).
- [16] Odom, T. W., Huang, J.-L., Kim, P., and Lieber, C. M. *Nature* **391**, 62–64 (1998).
- [17] Wildöer, J. W. G., Venema, L. C., Rinzler, A. G., Smalley, R. E., and Dekker, C. *Nature* **391**, 59–62 (1998).
- [18] Tans, S. J., Devoret, M. H., Dai, H., Thess, A., Smalley, R. E., Geerligs, L. J., and Dekker, C. *Nature* **386**, 474–477 (1997).
- [19] Dresselhaus, M. S., Dresselhaus, G., Charlier, J. C., and Hernández, E. *Philosophical Transactions of the Royal Society A* **362**, 2065–2098 (2004).
- [20] Blakslee, O. L., Proctor, D. G., Seldin, E. J., Spence, G. B., and Weng, T. *Journal of Applied Physics* **41**(8), 3373–3382 (1970).
- [21] Robertson, D. H., Brenner, D. W., and Mintmire, J. W. *Physical Review B* **45**(21), 592–595 (1992).
- [22] Treacy, M. M. J., Ebbesen, T. W., and Gibson, J. M. *Nature* **381**, 678–680 (1996).

## REFERENCES

---

- [23] Krishnan, A., Dujardin, E., Ebbesen, T. W., Yianilos, P. N., and Treacy, M. M. J. *Physical Review B* **58**(20), 14013–14019 (1998).
- [24] Wong, E. W., Sheehan, P. E., and Lieber, C. M. *Science* **277**, 1971–1975 (1997).
- [25] Despres, J. F., Daguerre, E., and Lafdi, K. *Carbon* **33**(1), 87–89 (1995).
- [26] Iijima, S., Brabec, C., Maiti, A., and Bernholc, J. *Journal of Chemical Physics* **104**(5), 2089–2092 (1996).
- [27] Yakobson, B. I., Brabec, C. J., and Bernholc, J. *Physical Review Letters* **76**(14), 2511–2514 (1996).
- [28] Tans, S. J., Verschueren, A. R. M., and Dekker, C. *Nature* **393**, 49–52 (1998).
- [29] Avouris, P. *Accounts of Chemical Research* **35**(12), 1026–1034 (2002).
- [30] Wu, Z., Chen, Z., Du, X., Logan, J. M., Sippel, J., Nikolou, M., Kamaras, K., Reynolds, J. R., Tanner, D. B., Hebard, A. F., and Rinzler, A. G. *Science* **305**, 1273–1276 (2004).
- [31] Yang, Z.-P., Ci, L., Bur, J. a., Lin, S.-Y., and Ajayan, P. M. *Nano Letters* **8**(2), 446–451 (2008).
- [32] Thostenson, E. T., Li, C., and Chou, T.-W. *Composites Science and Technology* **65**, 491–516 (2005).
- [33] Loh, O. Y. and Espinosa, H. D. *Nature Nanotechnology*, doi:10.1038/nnano.2012.40, Published online 2012-04-29.
- [34] Dequesnes, M., Rotkin, S. V., and Aluru, N. R. *Nanotechnology* **13**, 120–131 (2002).
- [35] Kinaret, J. M., Nord, T., and Viefers, S. *Applied Physics Letters* **82**(8), 1287–1289 (2003).
- [36] Lee, S. W., Lee, D. S., Morjan, R. E., Jhang, S. H., Sveningsson, M., Nerushev, O. A., Park, Y. W., and Campbell, E. E. B. *Nano Letters* **4**(10), 2027–2030 (2004).
- [37] Dujardin, E., Derycke, V., Goffman, M. F., Lefevre, R., and Bourgoin, J. P. *Applied Physics Letters* **87**, 193107 (2005).
- [38] Axelsson, S., Campbell, E. E. B., Jonsson, L. M., Kinaret, J., Lee, S. W., Park, Y. W., and Sveningsson, M. *New Journal of Physics* **7**, 245 (2005).
- [39] Yousif, M. Y. A., Lundgren, P., Ghavanini, F., Enoksson, P., and Bengtsson, S. *Nanotechnology* **19**, 285204 July (2008).
- [40] Jang, J. E., Cha, S. N., Choi, Y., Amaratunga, G. A. J., Kang, D. J., Hasko, D. G., Jung, J. E., and Kim, J. M. *Applied Physics Letters* **87**, 163114 (2005).
- [41] Jang, J. E., Cha, S. N., Choi, Y., Butler, T. P., Kang, D. J., Hasko, D. G., Jung, J. E., Jin, Y. W., Kim, J. M., and Amaratunga, G. A. J. *Applied Physics Letters* **93**, 113105 (2008).
- [42] Ghavanini, F. A., Lopez-Damian, M., Rafieian, D., Svensson, K., Lundgren, P., and Enoksson, P. *Sensors and Actuators A* **172**, 347–358 (2011).
- [43] Ghavanini, F. A. *Synthesis and characterization of vertically aligned carbon nanofibers for nanoscale devices*. PhD thesis, Chalmers University of Technology, (2011).
- [44] Cha, S. N., Jang, J. E., Choi, Y., Amaratunga, G. A. J., Kang, D.-J., Hasko, D. G., Jung, J. E., and Kim, J. M. *Applied Physics Letters* **86**, 083105 (2005).
- [45] Kaul, A. B., Wong, E. W., Epp, L., and Hunt, B. D. *Nano letters* **6**(5), 942–947 (2006).

- 
- [46] Lassagne, B., Tarakanov, Y., Kinaret, J., Garcia-Sanchez, D., and Bachtold, A. *Science* **325**, 1107–1110 (2009).
  - [47] Jensen, K., Kim, K., and Zettl, A. *Nature Nanotechnology* **3**(9), 533–537 (2008).
  - [48] Jensen, K., Weldon, J., Garcia, H., and Zettl, A. *Nano Letters* **7**(11), 3508–3511 (2007).
  - [49] Salvétat, J.-P., Kulik, A. J., Bonard, J.-M., Briggs, G. A. D., Stöckli, T., Méténier, K., Bonnamy, S., Béguin, F., Burnham, N. A., and Forró, L. *Advanced Materials* **11**(2), 161–165 (1999).
  - [50] [http://en.wikipedia.org/wiki/File:Schema\\_MEB\\_\(en\).svg](http://en.wikipedia.org/wiki/File:Schema_MEB_(en).svg), (2012-04-27).
  - [51] Voreades, D. *Surface Science* **60**, 325–348 (1976).
  - [52] Ohya, K. and Ishitani, T. *Journal of Electron Microscopy* **53**(3), 229–235 (2004).
  - [53] Seiler, H. *Zeitschrift für angewandte Physik* **22**, 249–263 (1967).
  - [54] Wei, X. L., Liu, Y., Chen, Q., and Peng, L. M. *Nanotechnology* **19**, 355304 (2008).
  - [55] Peroz, C., Babin, S., Machin, M., Anderson, E., Cabrini, S., Dhuey, S., and Harteneck, B. *Journal of Vacuum Science & Technology B* **27**(6), 3220–3225 (2009).
  - [56] <http://www.nanofactory.com/>, (2012-04-30).
  - [57] Svensson, K., Jompol, Y., Olin, H., and Olsson, E. *Review of Scientific Instruments* **74**(11), 4945–4947 (2003).
  - [58] Sader, J. E., Chon, J. W. M., and Mulvaney, P. *Review of Scientific Instruments* **70**(10), 3967–3969 (1999).
  - [59] Guldi, D. M., and Martin, N. *Carbon Nanotubes and Related Structures*. Wiley-VCH, Weinheim (2010).
  - [60] Thess, A., Lee, R., Nikolaev, P., Dai, H., Petit, P., Robert, J., Xu, C. H., Lee, Y. H., Kim, S. G., Rinzler, A. G., Colbert, D. T., Scuseria, G. E., Tomanek, D., Fischer, J. E., and Smalley, R. E. *Science* **273**, 483–487 (1996).
  - [61] Wagner, R. S. and Ellis, W. C. *Applied Physics Letters* **4**(5), 89–90 (1964).
  - [62] <http://www.nanocyl.com/>, (2012-04-27).
  - [63] Lu, K. L., Lago, R. M., Chen, Y. K., Green, M. L. H., Harris, P. J. F., and Tsang, S. C. *Carbon* **34**(6), 814–816 (1996).
  - [64] Moonosawmy, K. R. and Kruse, P. *Journal of the American Chemical Society* **130**, 13417–13424 (2008).
  - [65] Merkulov, V. I., Guillorn, M. A., Lowndes, D. H., Simpson, M. L., and Voelkl, E. *Applied Physics Letters* **79**(8), 1178–1180 (2001).
  - [66] Hertel, T., Martel, R., and Avouris, P. *Journal of Physical Chemistry B* **102**(6), 910–915 (1998).
  - [67] Falvo, M. R., Clary, G. J., Taylor II, R. M., Chi, V., Brooks Jr., F. P., Washburn, S., and Superfine, R. *Nature* **389**, 582–584 (1997).
  - [68] Lourie, O., Cox, D. M., and Wagner, H. D. *Physical Review Letters* **81**(8), 1638–1641 (1998).
  - [69] Lukić, B., Seo, J. W., Bacsá, R. R., Delpeux, S., Béguin, F., Bister, G., Fonseca, A., Nagy, J. B., Kis, A., Jeney, S., Kulik, A. J., and Forró, L. *Nano Letters* **5**(10), 2074–2077 (2005).
  - [70] Lee, K., Lukić, B., Magrez, A., Seo, J. W., Briggs, G. A. D., Kulik, A. J., and Forró, L. *Nano Letters* **7**(6), 1598–1602 (2007).

## REFERENCES

---

- [71] Bower, C., Rosen, R., Jin, L., Han, J., and Zhou, O. *Applied Physics Letters* **74**(22), 3317–3319 (1999).
- [72] Liu, J. Z., Zheng, Q., and Jiang, Q. *Physical Review B* **67**, 075414 (2003).
- [73] Arias, I. and Arroyo, M. *Physical Review Letters* **100**, 085503 (2008).
- [74] Nikiforov, I., Zhang, D.-B., James, R. D., and Dumitrica, T. *Applied Physics Letters* **96**, 123107 (2010).
- [75] Huang, X., Yuan, H., Liang, W., and Zhang, S. *Journal of the Mechanics and Physics of Solids* **58**, 1847–1862 (2010).